POLITECNICO DI TORINO

Dipartimento di Ingegneria dell'Ambiente, del Territorio e delle Infrastrutture
Corso di Laurea Magistrale
in Ingegneria per l'Ambiente e il Territorio

Tesi di Laurea Magistrale

EFFECT OF NEAR-SURFACE FLOW-PARTICLE INTERACTIONS ON SNOWFALL DEPOSITION IN ALPINE TERRAIN

Relatore
Manes Costantino

Correlatore
Lehning Michael

Candidato
Di Ciollo Chiara

Luglio 2018

A mio nonno . . .

Acknowledgements

I would like to thank people who gave me the opportunity to work on this project with an amazing team. So, first of all, I would thank Professor Michael Lehning, a scientist highly devoted to snow transport processes research (other than to many other fields involving cryosphere, natural hazards, atmospheric boundary layer flows, mountain hydrology and natural hazards, permafrost dynamics and renewable energy), Dr. Francesco Comola, who has been a constant and effective guide other than a very good student and researcher example to me. Secondly, I would ideally thank CRYOS group and the chance it gave to me to experience scientific team life inside EPFL. I would as well thank single CRYOS members for being nice friends, welcoming an motivating me in academic and social life. Thank also to the Erasmus+ (Swiss Mobility Programme) scholarship which allowed me realising the dream to join this university and amazing country. For the Italian side of my academic formation I would thank professor Costantino Manes, a fluid mechanics scientist from Politecnico di Torino, who is offering is advice and support.

Chiara Di Ciollo

July 2018

Abstract

Despite the growing body of literature in the field, dynamics and magnitude of preferential deposition ("the spatially varying deposition of solid and liquid precipitation due to topography-induced flow field modification close to the surface") are still largely unclear. Snow depth spatial distribution presents one of the major unknowns in the surface mass balance of alpine and polar regions, so in the hydrological response of a basin, other than in the avalanche hazard forecasting.
In a complex setting which is Alpine terrain, assessments of snow depth spatial distribution can not rely on point measurements and analytical methods. Together with orographic precipitation and wind-induced snow transport, snowfall preferential deposition is one of the main causes of inhomogeneous snow depth distribution in complex terrain.
This work aims at providing a better understanding of the influence of topographic and meteorological factors on preferential deposition; furthermore, it investigates to what extent preferential deposition process alone can explain the observed snow depth spatial variability in alpine terrain.
Field measurements and analytical methods do not allow to separate the effects of preferential deposition from those of precipitation gradients and drifting-blowing snow. We then rely on numerical modelling to investigate flow-particle interactions in the turbulent surface layer. In particular, in this study developed at CRYOS laboratory (EPFL), we couple large eddy simulation (LES) to solve large energy scales, Lagrangian stochastic model (LSM) to track particles trajectories and an immersed boundary method (IBM) to reproduce the real terrain model (DTM). Our study case is the Gaudergrat ridge (Grisons canton, Switzerland). To our knowledge this is the first time that such a comprehensive model is applied to a real topography.
Once validated the model against laboratory experiments found in literature, we initially perform a sensitivity analysis of the model results to the domain size, to test the influence of the boundary conditions on the deposition pattern in the area of interest. We then perform a series of simulations with increasing wind velocity and show that the snow cover distribution across the ridge becomes more and more inhomogeneous (typical low-high deposition alternation). Increasing advection, windward updraft increases and accumulation maxima move beyond the topographic peak in the wind direction. Our simulations also indicate that: dendritic crystals are more sensitive to flow advection than rounded particles, which enhances the preferential deposition pattern proving effective, while the assumption of inertialess (or passive) particles, often used in previous models, may lead to large errors for rounded grains.

We finally compare our model results to manual measurements of snow depth distribution on the Gaudergrat ridge and show that preferential deposition alone can not entirely explain the observed snow cover spatial variability: wind erosion of just deposited snowflakes, blowing and sublimation are, in fact, other important causes of inhomogeneous snow depth distribution.

Key words: Large Eddy Simulation, Lagrangian Stochastic Model, Immersed Boundary Method, preferential deposition, snow deposition patterns, Digital Terrain Model, snow depth variability, avalanches, alpine terrain, inertialess particles, dendritic snowflakes.

Abstract

Nonostante la crescente mole di letteratura nel settore, le dinamiche e l'entità della deposizione preferenziale ("the spatially varying deposition of solid and liquid precipitation due to topography-induced flow field modification close to the surface") rimangono ancora poco chiare. L'altezza di neve al suolo costituisce una delle maggiori incognite nel bilancio di massa della copertura nevosa nelle regioni alpine e polari, quindi nella valutazione delle risorse idriche, oltre che nella previsione del rischio valanghe.
In un contesto complesso come quello alpino, la valutazione della distribuzione spaziale dello spessore di neve al suolo, non può fare affidamento su misure puntuali o metodi analitici. Assieme alle precipitazioni orografiche e al trasporto di neve indotto dal vento, la deposizione preferenziale della precipitazione nevosa è una delle principali cause di eterogeneità nella distribuzione di neve su topografie complesse.
Questo lavoro punta a fornire una migliore comprensione dell'influenza dei fattori topografici e meteorologici sulla deposizione preferenziale della precipitazione nevosa. Esso vuole inoltre investigare in quale misura il processo di deposizione preferenziale può spiegare la variabilità osservata nello spessore del manto nevoso in territorio alpino.
Misure in campo e metodi analitici non consentono di separare gli effetti della deposizione preferenziale da quelli dei gradienti di precipitazione, o di drifting snow. Si fa pertanto, affidamento alla modellazione numerica per analizzare fenomeni di interazione fluido-particella nello strato turbolento dell'atmosfera superficiale. Nello specifico, in questa tesi, sviluppata al laboratorio di scienze della criosfera (CRYOS) dell'EPFL, sono stati combinati: Large Eddy Simulation (LES) per risolvere le scale del flusso turbolento a maggior contenuto energetico, Lagrangian Stochastic Model (LSM) per risolvere le traiettorie delle particelle nevose e Immersed Boundary Method (IBM) per riprodurre il reale modello digitale del terreno (DTM). Il caso studio è una cresta montuosa nel cantone dei Grigioni (Svizzera) nota col nome di Gaudergrat. Per quanto noto, questa tesi presenta la prima applicazione di un modello di tale dettaglio per la simulazione di precipitazione nevosa su una reale topografia.
Previa validazione del modello su esperimenti di laboratorio reperiti in letteratura, viene in prima istanza, eseguita un'analisi di sensibilità del modello alla dimensione del dominio, per valutare gli effetti delle condizioni al contorno sul pattern di deposizione nell'area di interesse. In secondo luogo viene condotta una serie di simulazioni con crescente intensità del vento da cui si notata che lo spessore del manto di neve a cavallo della cresta montuosa diventa conseguentemente sempre più disomogeneo (con tipica alternanza di zone di intenso accumulo e debole accumulo). Con l'aumento dell'intensità del vento, il moto ascensionale

sopravvento aumenta e sospinge le particelle nevose oltre la cresta, spostando così la zona di massimo accumulo nella direzione del vento. Dalle simulazioni emerge inoltre che le particelle modellate come cristalli dendritici sono più sensibili all'effetto di forze aerodinamiche rispetto a quelle sferiche; il pattern di deposizione preferenziale risulta infatti accentuato e più vicino a quello reale. Viene infine mostrato come l'assunzione modellistica di particelle prive di inerzia (o a comportamento passivo), spesso usata negli studi di letteratura, può condurre ad errori di stima nel caso di particelle sferiche. Per concludere questo studio, i risultati delle simulazioni sono confrontati con delle osservazioni in campo. Ciò mostra come il processo di deposizione preferenziale non possa, da solo, giustificare la variabilità spaziale dello spessore di neve misurato; l'erosione da parte del vento dei fiocchi di neve appena depositati, la loro reimmissione in sospensione e anche la loro sublimazione, sono infatti altri importanti processi che contribuiscono alla determinazione dell'eterogeneità dello spessore del manto nevoso.

Contents

List of Figures

List of Tables

1 Introduction

Snow is an important component of the water cycle and Earth climate equilibrium. Together with polar icecaps and glaciers, winter snow-cover extension and duration is in fact one of the most visible signs of climate change. Snow cover presence is not only relevant to alpine or polar regions, but also to several dry, lowland areas of Western America, Central Asia, Northern India and Souther Europe.
The hydrological cycle in alpine catchments presents a period of snow accumulation in the winter months and a period of snow melt from spring to late summer. This snow melt is one of the resources of drinking water and hydropower production. In alpine catchments the spatial snow depth distribution at the time of maximum accumulation is evidently a relevant control factor for the estimation of hydrologic response (distribution of snow water equivalent and run-off timing)Winstral et al. [2002], snow-melt flood, slope stability and avalanches forecasting (e.g. Schweizer et al. [2003]).

The snow-cover accumulation is a quite complex process. Internal snow pack phenomena like sintering or metamorphism that take place after snow settled, are not investigated in this study. We rather focus on surface processes that, acting at different scales during and after a storm, contribute to the inhomogeneous snow accumulation. Wind modification induced by topography, in addition to elevation and vegetation distribution leads to a variable snow precipitation and accumulation. These heterogeneity, weakly visible on the flattest terrain, are more remarkable on complex topography such as alpine terrain.
The main processes responsible for the snow depth spatial variability, decreasing the observation scale, are: *(a)* orographic precipitation [Colle et al., 2013], *(b)* preferential deposition [Vionnet et al., 2017] and *(c)* wind induced snow transport [Mott et al., 2010] but the relative contribution they give to the accumulation variability at different scales has not been clearly quantified.

We can distinguish between processes influencing the snow deposition which act before snowflakes touch the ground surface (or the pre-existing snow cover) and processes acting after snowfall deposition that redistribute snow grains on the surface.

In the first category we mention orographic precipitation *(a)*, which interests the scales of ambient atmospheric circulation (large scale): mechanical lifting of big moist air masses coming across a mountain, leads to their cooling and condensation with consequent precipitation (generally on the windward side). At smaller scale, we can observe precipitation gradients and seeder-feeder mechanism. *Precipitation gradients* are movement of maximum particles concentration toward the leeward side of the ridge because of strong near-surface wind modification and *seeder-feeder mechanism* is a micro-physical mechanism: seeding precipitation particles generated by a big storm, fall into a lower feeder cloud, orographically updrafted, and condense increasing their volume [Wang and Huang, 2017]. Another process precipitation-related (before snowflakes touch the ground), contributing to inhomogeneous snow accumulation is preferential deposition. With this *(b)* we refer to snowfall deposition process alone (without wind erosion and transport), that is related to topography and wind field characteristics. This phenomenon was for the first time isolated and named by Lehning et al. [2008] as one of the main factors playing for variable snow accumulation on alpine terrain at local scale (5-25 m). It is defined as "the spatially varying deposition of (solid and liquid) precipitation due to topography-induced flow field modification close to the surface" [Lehning et al., 2008].

Regarding processes acting after snowfall deposition, we mention drifting and blowing snow *(c)*. Once the snow flake reached the surface, small scale dynamics linked to the flow-particle and particle-particle interactions provide snow transport and redistribution significantly contributing to the final snow depth variability at small scale (centimetre). According to Lehning et al. [2008], drifting snow is a general term to account for reptation, creep, saltation and suspension. Saltation or aeolian transport then includes a complex series of near-surface processes: aerodynamic entrainment, rebounding, grain-bed collisions, ejection and wind modification/feedback [M. Nemoto, 2004]. Blowing snow, that is the snowflakes transported by wind in suspension, is often associated to these near surface processes.

Let's imagine a flow over a land with a certain horizontal mean velocity and snowflakes descending with a constant vertical velocity; if we additionally consider a complex topography such as an alpine terrain we will observe that, a part from turbulences induced by surface roughness, the terrain slope variability will cause zones of local flow convergence or divergence that will create vorticity and vary the vertical component of the flow velocity. As a consequence, this topography induced turbulence will vary the relative flow-particle velocity and so the final deposition (settling) velocity. Lehning et al. [2008] postulated that, increasing mean wind speed, the settling velocity reduced in the luff and increased in the lee side of the ridge leading to enhanced (preferred) deposition beyond the crest. Their results showed preferential deposition to be a significant contribution in lee-side snow accumulation variability at the ridge scale. Few years later Mott et al. [2010], investigating snow deposition and (wind induced) snow transport at different scales, underlined the importance of more accurate simulations. For this reason they used airborne and terrestrial laser scanners together with a dense meteorological stations network and found a negative correlation between typical winter areas of accumulation and higher horizontal (combined with lower down-ward) wind velocities. Following, Scipión et al. [2013], comparing snowfall observations (X-band radar) and snow accumulation measurements (laser scans), better understood that the only process of preferential deposition is not the first responsible for deposited snow spatial variability on alpine terrain. Snowfall variability over mountains summit can be a significant process at ridge scale (25-150 m). At local scale (5-25 m)[1], they observe that snowfall phenomenon becomes more heterogeneous close to the surface, where it is highly influenced by wind modification, than at hundred metres height. To be more clear about the scale of the domain and processes there involved, Mott et al. [2014] explain that at large scale the ambient atmospheric circulations in presence of high mountainous chain is forced to orographic lifting (cooling of moist air), condensation and consequent precipitation (orographic scale: windward enhanced snow precipitation); at a smaller scale a micro-physical mechanism, called seeder-feeder, may occur (intermediate scale: enhanced precipitation on hills-top). At slope scale, for discrete wind velocity, the maximum of particles concentration moves toward the leeward side of the ridge because of a stronger near-surface wind modification (possibly enhanced leeward precipitation).

According to Scipión et al. [2013] and Mott et al. [2010] spatial variability in snow accumulation on alpine terrain is higher than precipitation heterogeneity because of drifting of just deposited snow, that take place during strong wind events.

More recently, Wang and Huang [2017] used LES coupled with Lagrangian particles tracking to test atmospheric stability influence on deposition patterns. Their study suggested that the leeward preferential snow deposition increases with increasing velocity (as postulated by Lehning et al. [2008]). Vionnet et al. [2017], coupling Crocus and Meso-NH models, analysed separately different processes and suggested that spatial variability of precipitation is smaller than its accumulation variability when wind-induced snow transport is included.

Overall, despite the growing body of literature, studies still provide inconsistent results on the pattern of preferential deposition. Recently, Comola et al. [in preparation] adopted a comprehensive LES-LSM modelling with an immersed boundary method to perform scale analysis of snowfall deposition on ideal terrain (Gaussian hills). They suggest that the interplay between particle inertia, flow advection and gravity depends on the length scale and velocity scale of interest, i.e., on the hill size and on the wind velocity. Increasing wind field intensity enhances the snow accumulation in the lee ward hill side because flux advection becomes predominant on particles gravity, especially for larger scale hills. It is still unclear, however, if the results obtained by Comola et al. [in preparation] for Gaussian hills can be generalized to more realistic alpine terrain. Further development and application of numerical models is necessary to provide a better understanding on preferential deposition over alpine topography.

In the present work we aim at extending the initial findings of Comola et al. [in preparation] to a real alpine topography. In particular, we study how different flow field intensity and snow particle shape affect the pattern of preferential deposition. Furthermore, we compare model

[1] as defined in [Vionnet et al., 2017]

results to field measurements to infer the role of preferential deposition in the total snow depth spatial variability. In nature precipitation heterogeneity is quite challenging to measure since it occurs together with drifting and blowing, in a very shallow layer close to the surface. The most efficient way to decouple inhomogeneous precipitation and snow redistribution is then numerical. For this purpose, we propose a novel and comprehensive numerical model based on large eddy simulations with a Lagrangian stochastic particles tracking. We then add a real digital terrain model (using an immersed boundary method) to account for steepness variability and its consequences on the flow field.
Our study case is the Gaudergrat ridge, a ridge near Davos in the Western Swiss Alps, which has been studied for years from SLF[2] researchers [Lehning et al., 2008], [Mott and Lehning, 2010].

This study sheds light on the fundamental controls of snowfall preferential deposition over complex topography and may ultimately lead to better quantifications of the surface mass balance of alpine regions and avalanches forecasting via larger scale models.

The thesis is organized as follows: second theoretical chapter explanatory of the numerical method used, a third chapter for its validation; a fourth chapter explanatory of the model set-up and the chosen study case; a fifth chapter about simulations results, made up of a first part concerning sensitivity of the model to the domain size and a second part dealing with a sensitivity analysis to the flow field intensity plus other two limit simulations and a final chapter with conclusions.

[2]WSL (Swiss Federal Institute for Forest, Snow and Landscape Research) institute for snow and avalanches research.

2 Modelling turbulent flow and transport

2.1 Model Description

The numerical model used for this study comes from Albertson and Parlange [1999], Kumar et al. [2006] and later implementations. It can be defined as a Large Eddy Simulation code with an Immersed Boundary Method coupled with a Lagrangian Stochastic model that allows the simulation of precipitation and saltation processes separately to account for their respective effects on the snow depth spatial distribution. Here, we use the model exclusively to simulate snowfall deposition, in order to single out the role of preferential deposition. Before giving details about the setting of model parameters it is important to briefly explain how this model works. Note that a similar LES model has been previously used to investigate wind-farm effects on the atmospheric boundary layer [Sharma et al., 2017], turbulent flows over realistic urban surfaces [Giometto et al., 2016], to test linear and non-linear SGS models [Meneveau et al., 1996, Porté-Agel et al., 2000, Bou-Zeid et al., 2005], to perform scale and drifting analysis on ideal hills [Comola, 2017] and [Comola et al., in preparation].

2.2 Large Eddy Simulation

Having in mind that the surface layer (SL) is highly turbulent and turbulence is characterised by eddies size and associated kinetic energy, we can sketch large eddies as energy source while small eddies identifies the level at which energy dissipation happens (Figure 2.1).

The LES is then the method that allows solving large scale eddies (bigger than Δ, see section 2.3), i.e. energy containing ones, via the isothermal filtered Navier-Stokes equations [Orszag and Pao, 1975] while for small scale (or inertial sub grid scale) an effective parametrization is provided. Equation 2.1a expresses the momentum conservation, Equation 2.1b expresses the mass conservation, Equation 2.1c, Equation 2.1d and Equation 2.1e express boundary

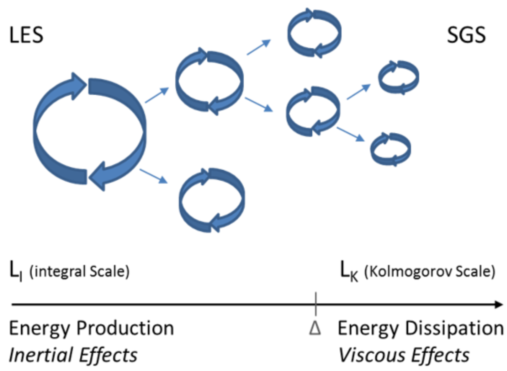

Figure 2.1: Sketch of eddies size and associated energy

conditions.

$$\frac{\partial \tilde{u}_i}{\partial t} + \tilde{u}_j \left(\frac{\partial \tilde{u}_i}{\partial x_j} - \frac{\partial \tilde{u}_j}{\partial x_i} \right) = -\frac{\partial \tilde{\pi}}{\partial x_i} - \frac{\partial \tau_{ij}^{SGS}}{\partial x_j} - \Pi_1 + \tilde{F}_i^{\Gamma_s} + \tilde{F}_i^p \qquad \text{in } \Omega \times [0,T], \tag{2.1a}$$

$$\frac{\partial \tilde{u}_i}{\partial x_i} = 0 \qquad \text{in } \Omega \times [0,T], \tag{2.1b}$$

$$\frac{\partial \tilde{u}_1}{\partial x_3} = \frac{\partial \tilde{u}_2}{\partial x_3} = \tilde{u}_3 = 0 \qquad \text{in } \Gamma_t \times [0,T], \tag{2.1c}$$

$$(\tilde{\mathbf{u}} \cdot \tilde{\mathbf{n}})\, \tilde{\mathbf{n}} = \tilde{\mathbf{u}}_n = 0 \qquad \text{in } \Gamma_s \times [0,T], \tag{2.1d}$$

$$\tilde{\mathbf{t}} = -\left[\frac{k\,(\tilde{\mathbf{u}} - \tilde{\mathbf{u}}_n)}{\ln\left(1 + \frac{\Delta}{z_0}\right)} \right]^2 \qquad \text{in } \Gamma_s \times [0,T]. \tag{2.1e}$$

where tilde indicates filtered quantities, $\tilde{u}_i$ stands for the velocity component in one of the three Cartesian directions ($i = 1,2,3$), $\tilde{\mathbf{n}}$ is the normal direction to the surface. $\tilde{\mathbf{u}}_n$ and $\tilde{\mathbf{t}}$ are the normal-to-surface velocity vector and the surface stress vector, respectively. Δ is the filter width and z_0 is the aerodynamic roughness length. Ω is the computational domain, $\tilde{\pi} = \tilde{p}/\rho + 1/3\,\tau_{ii}^{SGS} + 1/2\,\tilde{u}_i \tilde{u}_i$ is a modified filtered pressure field, ρ is a reference density, Π_1 is a pressure gradient that allows the simulated flow control, τ_{ij}^{SGS} represents the sub-grid scale stress tensor, $\tilde{F}_i^s$ expresses a forcing term due to the immersed boundary method, $\tilde{F}_i^p$ is a forcing term accounting for the effect of inertial particles on the flow for filtered scales. Knowing that the solution of turbulent fluid equations is affected by the closure problem[1] and that the model, according to Giometto et al. [2016], is not very sensitive to the choice of sub-grid closure model when used in combination with an immersed boundary, we adopted the simple static Smagorinsky's closure model [Stull, 2009] to evaluate the SGS term τ_{ij}^{SGS}, as a

[1] the condition in which the number of unknowns is larger than the number of equations and trying to eliminate/replace these unknowns with knowns variables we find even more unknowns [Stull, 2009]

function of LES-resolved quantity.

$$\tau_{ij}^{SGS} = -2\nu_t \tilde{S}_{ij} = -2\left(c_s\Delta\right)^2 |\tilde{S}|\tilde{S}_{ij}, \tag{2.2}$$

where, ν_t is the eddy viscosity, $\tilde{S}_{ij}$ is the filtered shear rate tensor, and c_s is the Smagorinsky coefficient that even being a function of the local properties of the flow, can be assumed constantly equal to $c_s = 0.16$ for homogeneous turbulence.

2.3 Immersed Boundary Method and Boundary Conditions

As mentioned, boundary conditions (bc) to the domain Ω are needed to solve the Navier-Stokes equations. At the domain top, stress-free and zero vertical velocity are imposed by the free-lid bc (Γ_t, equation 2.1c); at lateral boundaries, periodic condition are imposed (Γ_l), due to the Fourier expansions used in the pseudo spectral approach, while an immersed boundary method is used to apply the surface boundary conditions.
In this model implementation has been chosen to represent the surface topography (ideal or real one) using an immersed boundary method (IBM) which allows to solve the turbulent flow equations on Cartesian grids with a small impact on the computational cost [Salesky et al., 2016]. An immersed boundary is defined by the distance function $\tilde{\Phi}\left(x,y,z\right)$, which identifies two half-space: Ω_s (where $\tilde{\Phi}\left(x,y,z\right) < 0$) below the topographic surface, where we want the velocity to go to zero, and Ω_f ($\tilde{\Phi}\left(x,y,z\right) > 0$) above it (in the fluid region). This immersed boundary method plays in the momentum balance equation 2.1a via $\tilde{F}_i^{\Gamma_s}$ term. Moreover, LES is not a wall-resolving simulation, so a wall model must be imposed close to the IBM interface in order to recover the correct velocity profile [Salesky et al., 2016]. We can then say that bottom boundary conditions, are those for velocity and shear at the IBM interface: no-slip bc (equation 2.1d) and law of the wall (equation (2.1e), in the normal direction to the surface, where $\Delta = \left(\Delta_x \times \Delta_y \times \Delta_z\right)^{1/3}$ is the filter width).

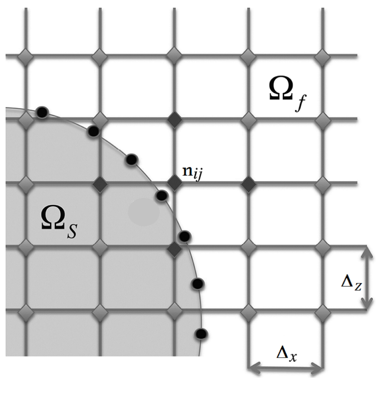

Figure 2.2: Sketch of an idealized immersed boundary and a Cartesian numerical grid

As mentioned in Comola et al. [in preparation], it is worth to note that because solution at equations 2.1 has discontinuous first derivatives, in any horizontal plane intersecting the lower boundary Γ_s, the spectral representation of the flow field results in strong Gibb's oscillations at the interface ($\tilde{\Phi}\left(x, y, z\right) = 0$). In order to attenuate this undesirable effect, we perform a Laplacian smoothing of the velocity field in Ω_s before the spectral differentiation step [Tseng et al., 2006]. [For further details on this comprehensive method and its previous applications, see Salesky et al. [2016], Comola et al. [in preparation, and all references there in]]

2.4 Lagrangian Stochastic Model

As anticipated, Lagragian stochastic model (LSM) completes the modelling of the full turbulent spectrum, ensuring accurate particles dispersion simulations by providing evolution equations of the sub-grid-scale velocity of a fluid parcel in turbulent motion. The stochastic evolution equation for the velocity fluctuations used in this study is that derived by Thomson [1987] based on the local ensemble-mean velocity and velocity variances of the flow . More recent LES studies [Weil et al., 2004] adopted a modified version of Thomson [1987] model, in which the ensemble-mean velocity is replaced by the LES-resolved velocity and the velocity variances estimations is based on the SGS closure model.

Under the hypothesis of isotropic SGS velocity component, the evolution of the SGS velocity along a fluid particle's trajectory $\mathbf{X}_f$ can be expressed as

$$\mathrm{d}U_i^{SGS} = -\frac{\alpha U_i^{SGS}}{T_f}\mathrm{d}t + \frac{1}{2}\left(\frac{1}{\sigma^2}\frac{\mathrm{d}\sigma^2}{\mathrm{d}t}U_i^{SGS} + \frac{\partial \sigma^2}{\partial x_i}\right)\mathrm{d}t + \left(\frac{\alpha 2\sigma^2}{T_f}\right)^{1/2}\mathrm{d}\xi_i \tag{2.3}$$

where $\sigma^2 = 2e/3$ is the SGS velocity variance, directly proportional to the SGS turbulence kinetic energy $e = (\epsilon\Delta/c_\epsilon)^{2/3}$ [Pope, 2001]; ϵ is the energy dissipation rate and $c_\epsilon = 0.93$ under the hypothesis of neutral and unstable stratification. According to Kolmogorov [1941]'s assumption (over sufficiently large time intervals, the mean energy production equals the mean energy dissipation) we can compute the turbulence dissipation ϵ averaging the energy production term P over sufficiently long time intervals as

$$\epsilon \approx \langle P\rangle = \langle -\tau_{ij}\tilde{S}_{ij}\rangle. \tag{2.4}$$

for each grid node. Still explaining the terms in Equation 2.3, $\alpha \in [0;1]$ is then the SGS fraction of the total turbulence kinetic energy, $\mathrm{d}\xi_i \sim \mathcal{N}(0, \mathrm{d}t)$ is a random number sampled from a normal distribution of zero mean and variance $\mathrm{d}t$ and $T_f = 2\sigma^2/C_0\epsilon$ is the velocity autocorrelation time scale.

At this point, to compute the Lagrangian trajectories of the snow particles we refer to a forces balance between drag and gravity. Given $X_{p,i}$, the particle position and $U_{p,i}$, the Lagrangian particle velocity, we can write

$$\frac{\mathrm{d}X_{p,i}}{\mathrm{d}t} = U_{p,i}, \tag{2.5}$$

$$\frac{\mathrm{d}U_{p,i}}{\mathrm{d}t} = \frac{\Delta_u}{t_p} - g\delta_{i3}. \tag{2.6}$$

where $\Delta_u = \tilde{u}_i + U_i^{SGS} - U_{p,i}$ is the difference between the flow velocity and the particle velocity, with U_i^{SGS} the SGS flow velocity felt by the heavy particle (snow). As we can imagine, a heavy particle (snow grain, in this case) trajectory $\mathbf{X}_p$ does not generally coincide with the trajectory of the fluid $\mathbf{X}_f$ that provides its transport; for this reason equation (2.3) should be modified to predict the turbulence fluctuations along the heavy particle trajectory. For this purpose, we followed the suggestion of Wilson [2000] of reducing the velocity autocorrelation time scale T_f, that then becomes T_p

$$T_p = \frac{T_f}{\sqrt{1 + \left(\frac{\beta U_{p,3}}{\sigma}\right)^2}}, \tag{2.7}$$

where $U_{p,3}$ is the vertical component of the Lagrangian particle velocity, $C_0 = 4 \pm 2$ is a dimensionless constant, $\beta \approx 2$ is a calibration coefficient suggested by Wilson [2000].

Continuing explaining terms of the equation (2.6), t_p is the particle relaxation time[2] and can be expressed as

$$t_p = \frac{\rho_p d_p^2}{18\mu} \frac{1}{f\left(\mathrm{Re_p}\right)}, \tag{2.8}$$

where $\mathrm{Re_p}$ is the particle Reynolds number and $f\left(\mathrm{Re_p}\right) = 1 + 0.15{\mathrm{Re_p}}^{0.687}$ [Clift et al., 2005]. An alternative form of the equation (2.8) can be given if we want to account for the real non-sphericity of particles. To this purpose and Loth [2008] proposed a correction of the relaxation time for dendritic crystals. From experimental investigations they saw that these crystals present a much smaller relaxation time, than rounded grains, which is well approximated

[2] time taken for a particle to come to equilibrium with its surroundings [Reeks, 1983]

using $f\left(\mathrm{Re_p}\right) = f_s\left[1 + 0.15\left(\mathrm{Re_p} C_s/f_s\right)^{0.687}\right]$ with $f_s = 3.1$ and $C_s = 25$.

At this point, a time integration of equation (2.6) with a second-order accurate Verlet scheme [Verlet, 1967] is needed; then, after updating particle position and velocity, we compute the forcing term $\tilde{F}_i^p$ of the initial equation (2.1a) as

$$\tilde{F}_i^p(\mathbf{x}, t) = -\sum_{n=1}^{N_p} f_i^n\left(\mathbf{X}_p^n, t\right)\delta\left(\mathbf{x} - \mathbf{X}_p^n\right), \tag{2.9}$$

where N_p is the total number of particles, $\delta\left(\mathbf{x} - \mathbf{X}_p^n\right)$ is a Dirac delta function centred in the particle's position, and $f_i^n\left(\mathbf{X}_p^n, t\right)$ is the drag force that the flow exerts on the n^{th} particle, i.e.

$$f_i\left(\mathbf{X}_p, t\right) = \frac{\rho_p}{\rho}\frac{\Delta_u}{t_p}. \tag{2.10}$$

2.5 Dimensionless forms

It is usual in physical problems to refer to dimensionless formulations in order to make equations more general, and identify their dependence on reference scales such as length and velocity. In this case, the filtered Navier Stokes equation (2.1a), divided by a combination of U (a reference velocity, usually free-stream v.) and L (a reference length scale, usually the hill/topography characteristic size) becomes

$$\frac{\partial \hat{\tilde{u}}_i}{\partial \hat{t}} + \hat{\tilde{u}}_j\left(\frac{\partial \hat{\tilde{u}}_i}{\partial \hat{x}_j} - \frac{\partial \hat{\tilde{u}}_j}{\partial \hat{x}_i}\right) = -\frac{\partial \hat{\tilde{\pi}}}{\partial \hat{x}_i} - \frac{\partial \hat{\tau}_{ij}^{SGS}}{\partial \hat{x}_j} - \hat{\Pi}_1 + \hat{\tilde{f}}_i^{\Gamma_s} - \frac{\rho_p}{\rho}\sum_{n=1}^{N_p}\frac{\Delta_{\hat{u}}^n}{\mathrm{St}^n}\delta\left(\hat{\mathbf{x}} - \hat{\mathbf{X}}_p^n\right). \tag{2.11}$$

where the symbol ˆ (hat) over a variable stands for dimension-less and $\mathrm{St} = t_p U/L$ is the Stokes number.

Likewise, the particle equation of motion (2.6) becomes

$$\frac{\mathrm{d}\hat{U}_{p,i}}{\mathrm{d}\hat{t}} = \frac{\Delta_{\hat{u}}}{\mathrm{St}} - \frac{1}{\mathrm{Fr}^2}\delta_{i3}, \tag{2.12}$$

where $\mathrm{Fr} = U/\sqrt{gL}$ is the Froude number.

Equations (2.11) and (2.12) indicate that St and Fr^2 are the dimensionless numbers that control the flow and particle dynamics. In other words: increasing St, particle dynamics become less and less driven by advection, while increasing Fr^2 the control of gravity on particle trajectories diminishes.

3 Model Validation

As due for any numerical model implementation, before applying it to the study of preferential deposition on alpine topography, it is worth to provide a validation of its accuracy. For this purpose, as already done by Comola [2017], we tested the model following the set-up of one of the wind tunnel experiments of dust deposition run by Goossens [1996]. We reproduced the ideal topography by six Gaussian hills, all 4 cm high (H) and 28 cm wide (L)[1] in order to respect the length ratio $L/H = 7$. The domain, L_x x L_y x L_z = 168 x 84 x 50 cm³, is described by a Cartesian grid of $N_x = 128$, $N_y = 64$, and $N_z = 99$ nodes. To reach flow condition similar to those described in Goossens [1996], like wind tunnel free stream velocity $U_\infty \approx 1.6 m/s$, we first performed a LES simulation alone. In a following simulation we added dust particles with a density $\rho_p = 2600\ kg/m^3$ and a diameter sampled from a log-normal distribution $d_p \sim log\mathcal{N}(\langle d_p\rangle, \sigma_d)$, where $\langle d_p\rangle = 30\ \mu$m and $\sigma_d = 7\ \mu$m. Given the very small time step ($2x10^{-4}$ s), the duration of the simulation ($60s$[2]) is smaller than that of the wind tunnel experiment . In order to compare the two results, values showed are normalised by the mean ($\tilde{\delta} = D/\ \langle D\rangle$).

Figure 3.1 represents the dust concentration. Figure 3.2 shows velocity among the three principal directions and we see that the free stream velocity simulates the reference experiment one (192 cm/s [Goossens, 1996]). Figure 3.3 shows deposition patterns over the hills series. Figure 3.4 compares measured dust deposition by Goossens [1996] and simulated one.

[1] L is the distance between two adjacent hilltops

[2] which is $30 * T$, with $T = L_z/u^*$ the eddy turnover time: time that larger eddies need to cross the domain

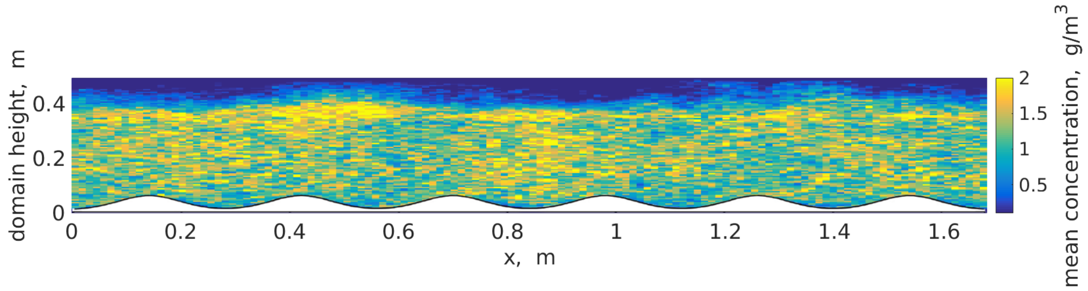

Figure 3.1: Simulated dust concentration in the mid-channel vertical section. The values showed are averaged among simulation time and y direction.

Dust concentration is showed in the middle vertical wind tunnel section. The values given in g/m^3 are averaged among the simulation period.

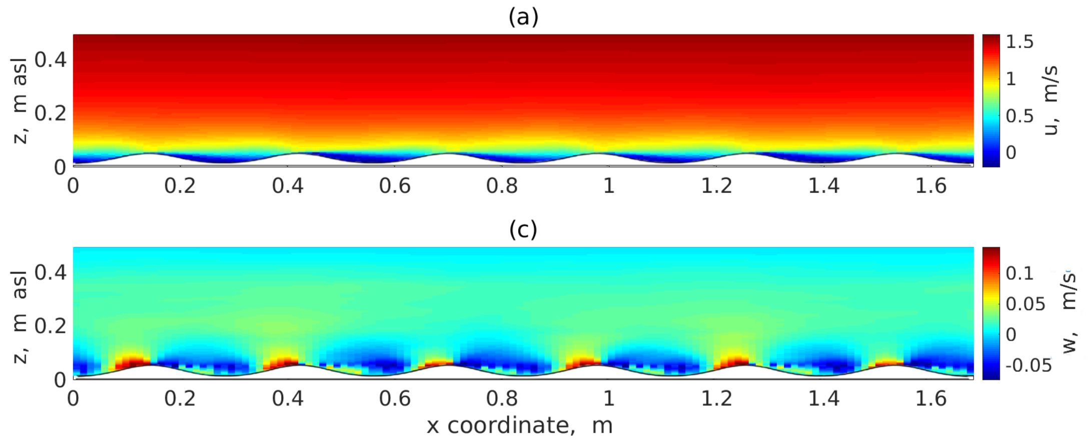

Figure 3.2: Simulated wind intensity over the Gaussian hills series. The values showed, x-wise velocity (a), and vertical velocity (c), are averaged among the total simulation time and y dimension.

Most significant velocity components are x-wise and z-wise ones. In the first case (Figure 3.2a) we can in fact read the major component of the free-stream velocity ($1.5m/s$), while Figure 3.2c shows intense updraft zones in the wind ward side and more extensive downdraft zones after the summit: stagnation zones are typical in the valleys between two hills and that do not perturb the flow-field above 20 cm height.

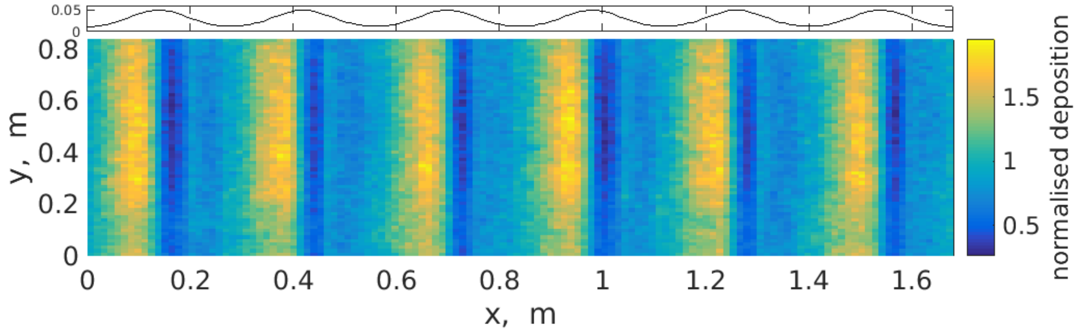

Figure 3.3: Normalised values of simulated deposition over the gaussian hills series. On the top: topographic profile of the hills series

Figure 3.3 shows peak accumulation on de wind-ward slopes followed by a significant drop in deposition at the slope inflection point. The lowest deposition values (blue range) are visible between the hilltops and the lee-ward inflection points.

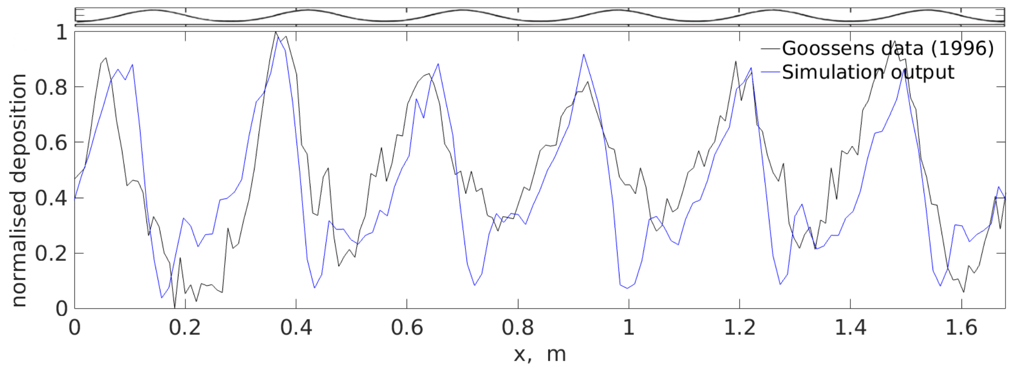

Figure 3.4: Measured dust deposition (according to Goossens [1996]) against simulated deposition. On the top: topographic profile of the hills series

We can observe that overall our LES-LSM-IBM model (blu line) predicts quite effectively the dust deposition over this artificial topography Figure 3.4. Going more into the detail we can notice that simulation output profile is much more regular (almost periodic behaviour) than the real experiment deposition profile (red line). In particular, the estimated minima deposition in the two central hills are lower and also closer to the hills summit than measured ones. Experimental minima deposition is found to happen slightly lower on the lee-slope, toward the inflection point. This might be partly due to a larger sheltering effect in the model probably caused by higher wind velocity.

4 Case study and model set-up

As announced in the introduction our aim is to investigate if snow preferential deposition on real terrain does respect what previously understood on idealized topographies by Comola et al. [in preparation] and how much of the total snow depth variability can be explained by preferential deposition alone. For this purpose we selected our case study in the eastern part of Switzerland, in the Grisons canton at the latitude of 46.856° Nord and Longitude 9.7958° East, at 6.5 km air distance from Davos (Figure 4.1). The ridge we are going to focus on, the Gaudergrat ridge, lays on a SW-NE direction, has a quite sharp shape with steep slopes and its maximum altitude is around 2305 m (Figure 4.2 and 4.3). The typical wind flow observed is NW-SE oriented with variable intensity. For the benchmark simulation we assumed a mean flow field velocity of around 6 − 7 m/s, following previous studies on the same area (as [Lehning et al., 2008] and [Mott and Lehning, 2010]).

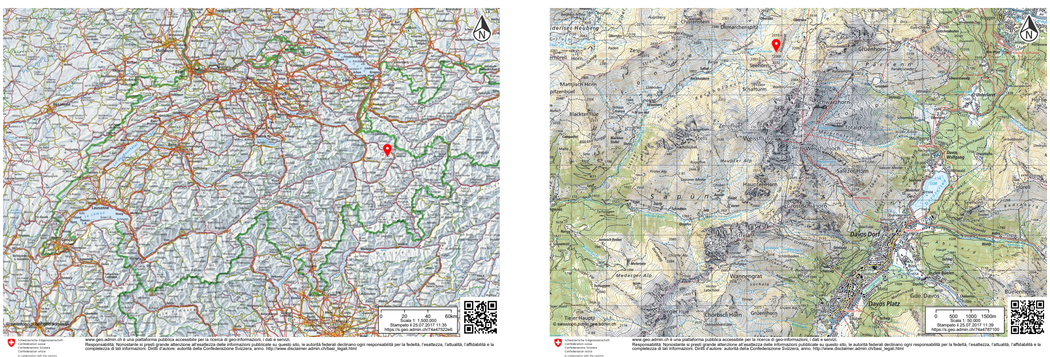

Figure 4.1: Site location in Switzerland, different scales

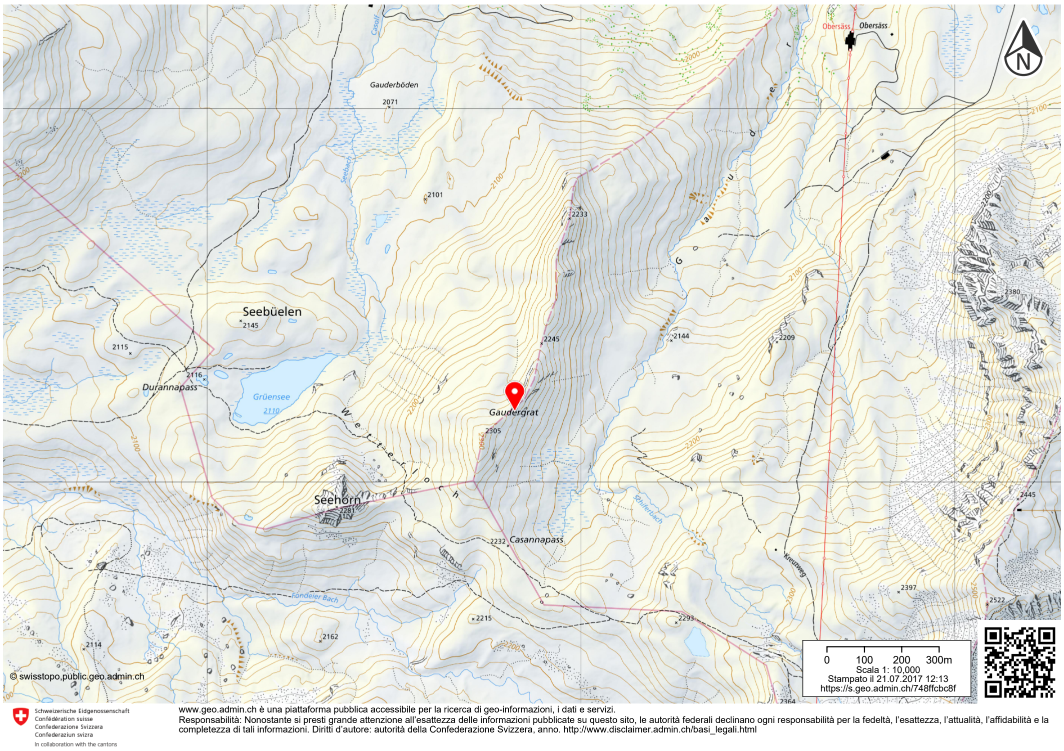

Figure 4.2: Gaudergrat ridge

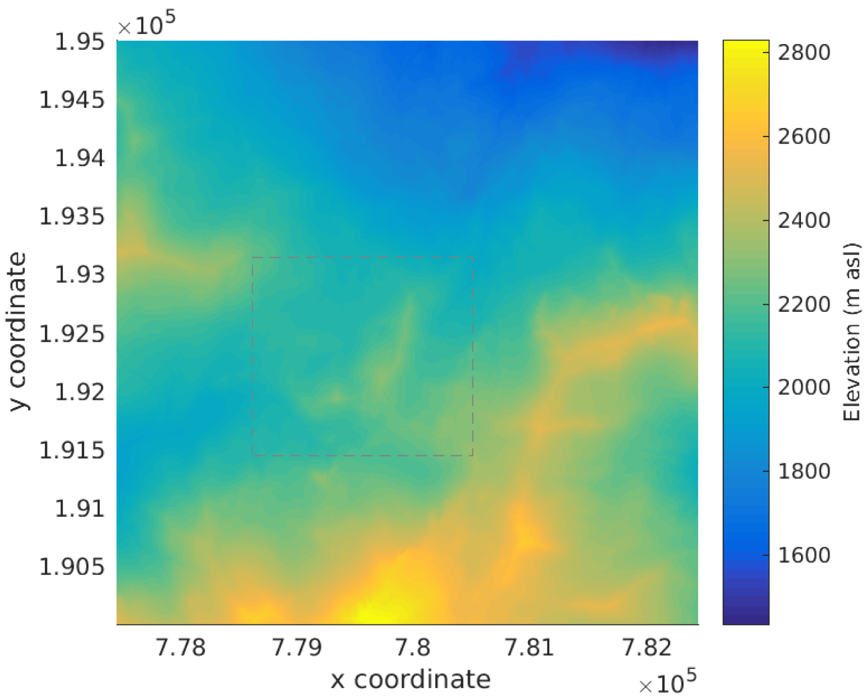

Figure 4.3: Original DTM of the entire region

We used the digital terrain model (DTM) of the case study to generate the immersed boundary in the LES simulations. First of all, a re-sampling of the original DTM has been necessary: its resolution can not be much higher than the numerical grid resolution to avoid numerical errors linked to the solution of the LES equations with a spectral method (Table 4.2). Secondly, we needed to modify its boundaries according to the immersed boundary periodic b.c. requirement. The DTM has equal side length in the x and y directions and the Gaudergrat ridge is located in the central region. The periodic surface generated has a constant elevation at the boundaries, equal to the mean elevation of the real topographic boundaries. We then generate a buffer zone in order to smooth the transition from the constant value of the periodic boundaries to the real topography elevation. A weighted distance average has been applied. The modification of the topography inevitably affects the flow field in the vicinity of the boundaries. The computational domain should thus be large enough to avoid significant modifications of the flow field around the ridge and yet small enough to ensure a sufficient spatial resolution. We seek the best trade off between accuracy and resolution through a sensitivity analysis of the model results to the domain size. Starting from a target domain of 4 km^2 (E1) centred on the ridge, we gradually increased the area (E2 and E3) and compared the simulated deposition patterns. A summary of these simulations is given in Table 4.1 while results will be shown in the next Chapter 5.

The core analysis of this study, is the sensitivity analysis of the modelled deposition pattern to the flow field intensity. Starting from the reference case (E1) we reduced the wind speed to half of its original value (E4) and then we doubled it (E5).

The numerical model (described in the previous Chapter 2) requires as input parameters: the domain size, the numerical grid resolution, the time stepping, the flow and particles characteristics (as friction velocity, pressure forcing factor, particle's density and diameter). We set a Cartesian grid of $N_x = N_y = 128$ and $N_z = 99$ nodes (x, y and z directions) to solve the LES equations. In all cases the domain has a square basis ($L_x = L_y$) and an height that is a half of the base side ($L_z = L_y /2$). The plane of precipitation release is located at $0.8L_z$. The simulated snowfall is constant over time (10 mm/h) and uniform over the plane of release. Snowflakes are simplified by mean of spherical particles (from E1 to E5) with an equivalent diameter of $d_p = 2\ mm$ and a density $\rho_p = 500$ kg/m^3 (reduced to account for the real non-spherical properties of snow flakes). According to the observations by Magono and Nakamura [1965] and Passarelli Jr and Srivastava [1979], natural snowflakes' effective density decays (approximately) with the square of their equivalent diameter. It follows a particle relaxation time $t_p \approx 0.5$ s. The flow field average direction and intensity are controlled by the pressure gradient, which is set in order to reproduce the flow conditions of studies conducted on this area (Lehning et al. [2008], [Mott and Lehning, 2010]). A summary of this second round of simulations is given in Table 4.2 while results will be shown in the next Chapter 5.

Finally we performed a two additional simulations (E6 and E7 in Table 4.3) in order to investi-

gate the limits of two modelling assumptions often used in previous studies of preferential deposition, i.e., that of inertialess particles and that of spherical particles.
In simulation E6 particles dynamics are modelled such as they had no inertia but a constant downward settling velocity (as assumed by Lehning et al. [2008]), set equal to 1 m/s following recent studies by Garrett and Yuter [2014]. In simulation E7 we account for dendritic shape of the crystals using the correction to the drag law proposed by Loth [2008]. Accordingly, the relaxation time of dendritic crystals (Equation (2.8)) is smaller than that of spheres and equal to $t_p \approx 0.05$ s. Comola et al. [in preparation] performed similar simulations to investigate the effects of inertia and particle shape on the deposition pattern over Gaussian hills at different spatial and temporal scales.

For each simulation (from E1 to E7), we first let the flow evolve until the overall turbulence kinetic energy in the domain reaches a stationary condition. Afterwards, we start entraining snowflakes uniformly from the upper boundary of the computational domain. Every time a flake hits the surface we update the deposition pattern. When particles cross lateral boundaries they are re-injected from the opposite side of the domain, consistently with the periodic boundary conditions of the flow. The duration of each simulations is around 840 s (14 min).

Name	$\mathbf{L_x}$	$\mathbf{L_y}$	$\mathbf{L_z}$	$\mathbf{\Delta_x}$	$\mathbf{\Delta_y}$	$\mathbf{\Delta_z}$	$\mathbf{\Delta_t}$
E1	2000	2000	1000	15.6250	15.6250	10.1010	0.005
E2	3000	3000	1500	23.4375	23.4375	15.1515	0.005
E3	4000	4000	2000	31.2500	31.2500	20.2020	0.005

Table 4.1: List of simulations performed to study the sensitivity of the deposition process to the domain size. All lengths are given in (m) and times in (s).

Name	$\mathbf{L_x}$	$\mathbf{L_y}$	$\mathbf{L_z}$	$\mathbf{\Delta_x}$	$\mathbf{\Delta_y}$	$\mathbf{\Delta_z}$	$\mathbf{\Delta_t}$	$\mathbf{U_\infty}$	**St**	$\mathbf{Fr^2}$
E1	2000	2000	1000	15.6250	15.6250	10.1010	0.005	7.3812	0.0664	0.0999
E4	2000	2000	1000	15.6250	15.6250	10.1010	0.005	3.7642	0.0339	0.0260
E5	2000	2000	1000	15.6250	15.6250	10.1010	0.005	14.6528	0.1318	0.3937

Table 4.2: List of simulations performed to test the sensitivity of the deposition process to the flow field intensity (here represented by Stokes and Froude numbers). All lengths are given in (m), times in (s), and velocities in (m/s).

Name	$\Delta_{\mathbf{x}}$	$\Delta_{\mathbf{y}}$	$\Delta_{\mathbf{z}}$	$\Delta_{\mathbf{t}}$	$\mathbf{U}_{\infty}$	Particle type	particle inertia
E1	15.6250	15.6250	10.1010	0.005	7.3812	spheric	inertial
E6	15.6250	15.6250	10.1010	0.005	7.3812	spheric	inertia-less
E7	15.6250	15.6250	10.1010	0.005	7.3812	dendritic	inertial

Table 4.3: List of simulations performed to test the sensitivity of the deposition process to particles inertia and shape. All lengths are given in (m), times in (s), and velocities in (m/s).

5 Results

In this section we include a first sensitivity analysis of the model to the domain size and a second part consisting in the investigation of flow intensity effects on deposition patterns. Further investigations are made on the particle inertia and particle shape effects on deposition patterns.

5.1 Sensitivity analysis to the domain size and grid resolution

Because the periodic b.c. of the LES model require a modification of the real topography close to the boundaries (see Section 4 and Section 3), we perform a sensitivity analysis of the model results to the domain size to seek the best trade off between accuracy and spatial resolution. We carried out a sensitivity analysis of the model to the artificial boundaries reconstruction, progressively enlarging the domain size. Simulations E1, E2, E3 (respectively *Gaudergrat1*, *Gaudergrat2*, *Gaudergrat3*) were set in order to have approximately the same flow conditions (wind field intensity and direction). Figure 5.1, Figure 5.2 and Figure 5.3 give a global view of the topography variation when accounting for larger domain.
For each case we show a 2D map of the deposition pattern (Figure 5.5,Figure 5.7, Figure 5.9) and then, focusing on four topographic sections, snow depth and averaged wind velocity will be compared among the three different domains (from Figure 5.10 to Figure 5.15).

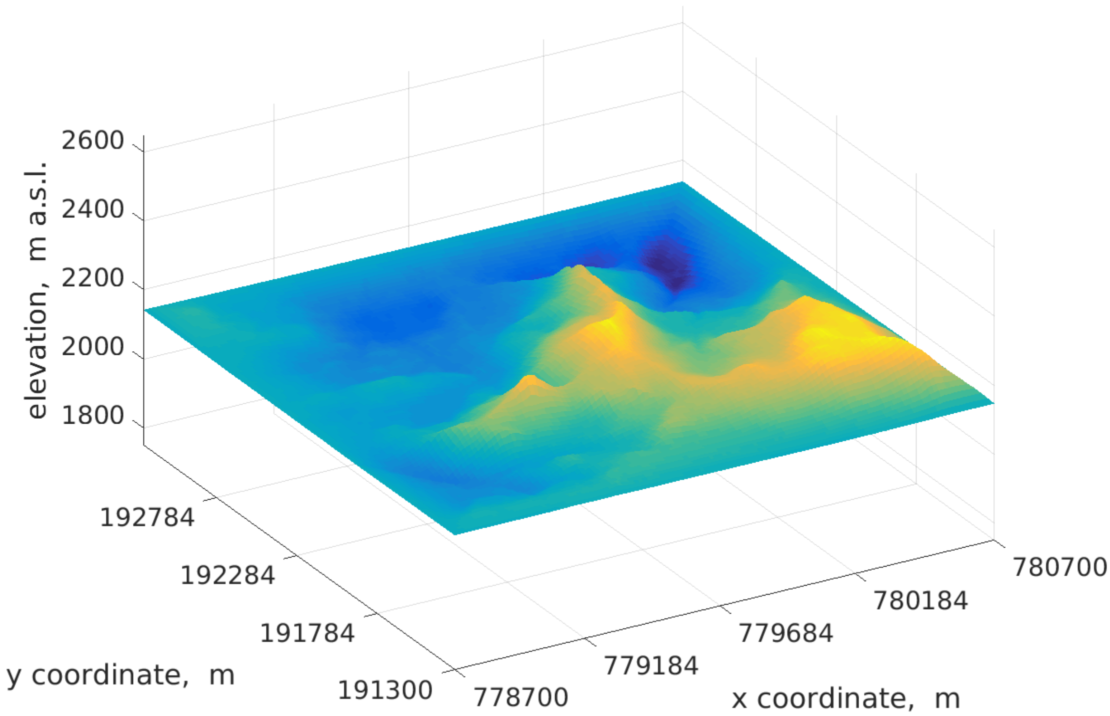

Figure 5.1: Digital Terrain Model of Gaudergrat ridge (periodic boundaries), 4 km² area. Vertical dimension is not in scale with x and y dimensions.

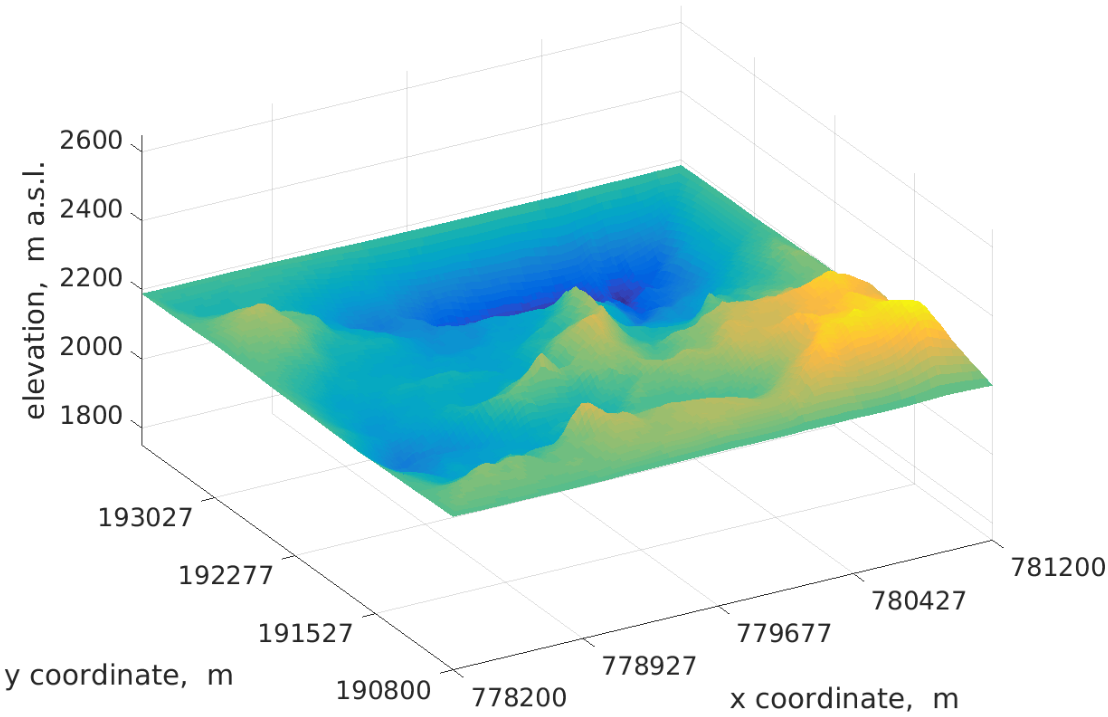

Figure 5.2: Digital Terrain Model of Gaudergrat ridge (periodic boundaries), 9 km² area. Vertical dimension is not in scale with x and y dimensions.

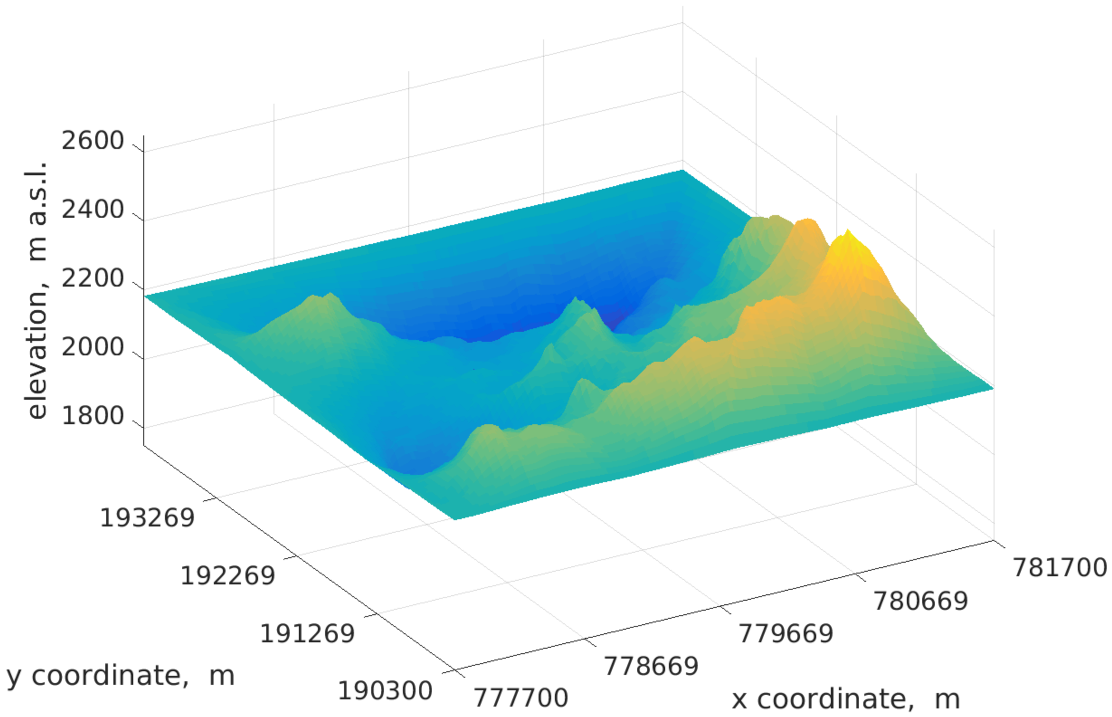

Figure 5.3: Digital Terrain Model of Gaudergrat ridge (periodic boundaries), 16 km² area. Vertical dimension is not in scale with x and y dimensions.

- E1: *Gaudergrat1*
  The region shown in Figure 5.4 consists of a 4 km² square area with a computational grid resolution of $15{,}625^2$ m² and a maximum elevation gain of 400m. The wind direction in the area is generally NW-SE oriented; roughly perpendicular to the steepest part of Gaudergrat's ridge. Simulated wind velocity is not higher than 8 m/s (as explained in Section 4). The deposition resulting from the simulation of precipitation (Figure 5.5) is divided by the spatial mean of the deposition pattern to allow for a more precise comparison among the different model configurations.

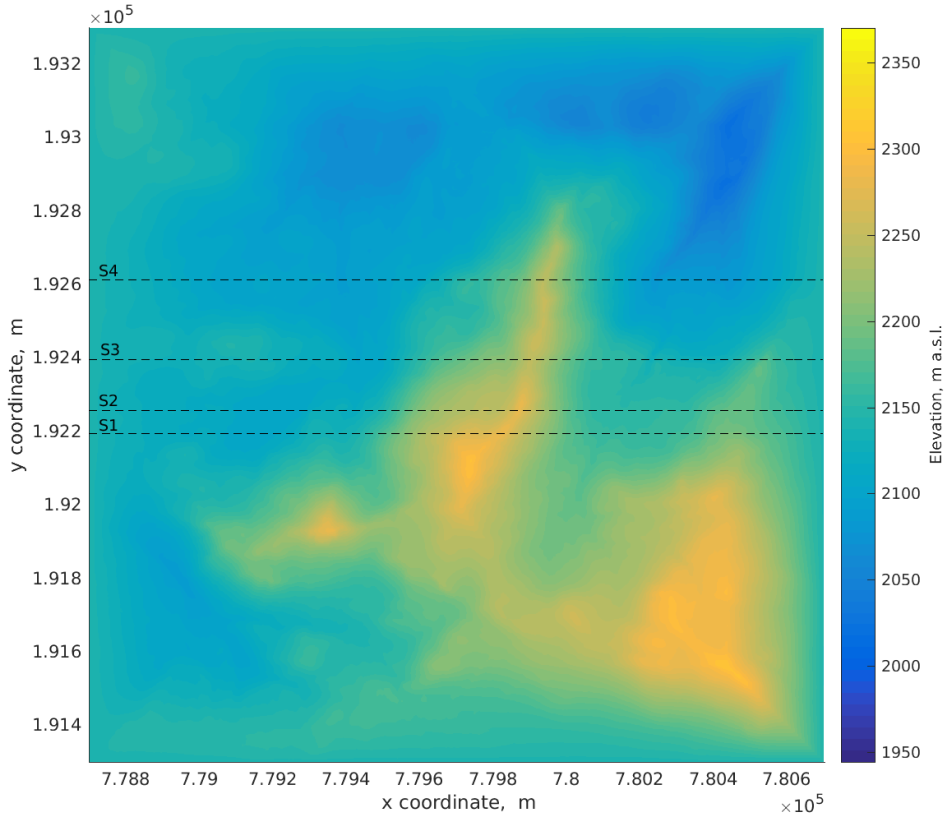

Figure 5.4: Digital Terrain Model of Gaudergrat ridge - periodic boundaries, 4 km² area.

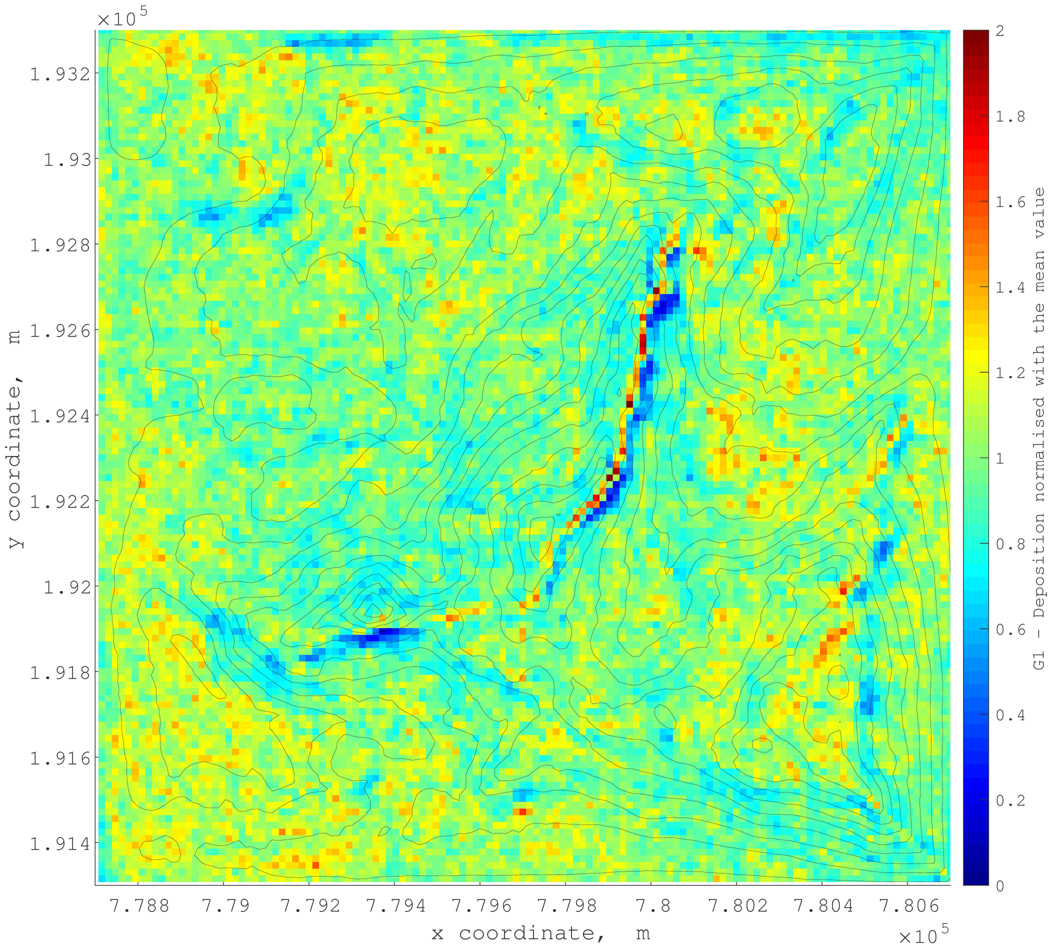

Figure 5.5: Deposition patterns on the 4 km² region around the Gaudergrat ridge. Black lines match same elevation points.

- E2: *Gaudergrat2*

  The region shown in Figure 5.6 consists of a 9 km² square area with a computational grid resolution of 23.438² m² and a maximum elevation gain smaller than 800 m. The wind direction in the area is, as before, roughly perpendicular to the steepest part of Gaudergrat's ridge. Simulated wind velocity is not higher than 7 m/s.

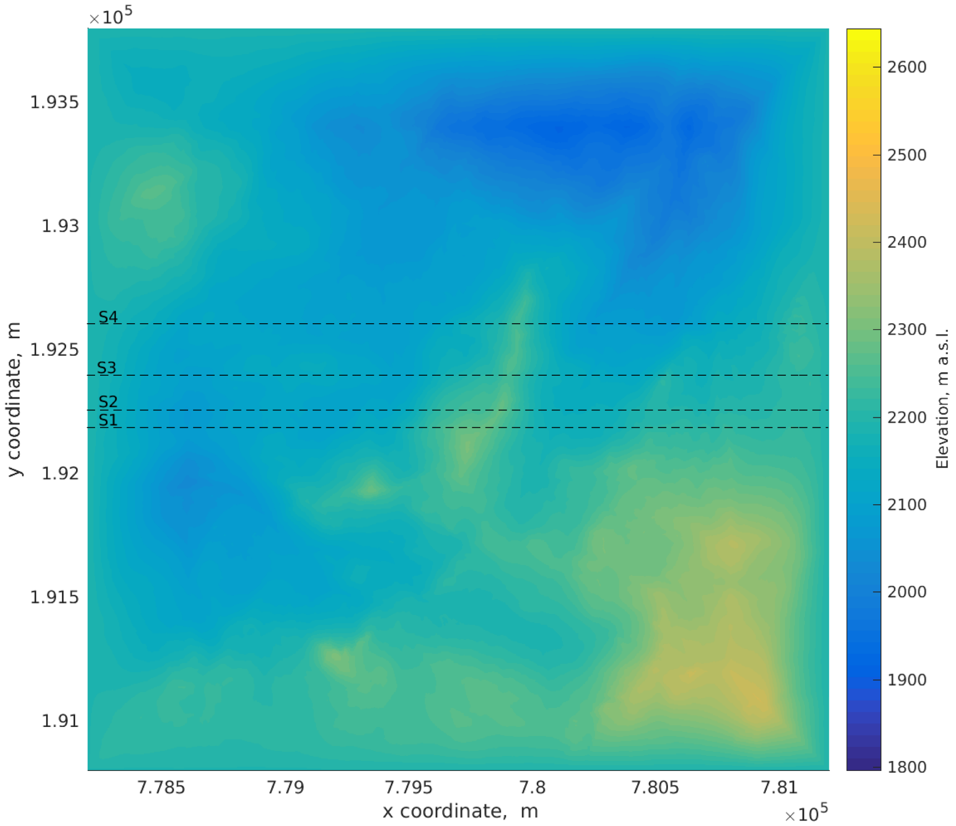

Figure 5.6: Digital Terrain Model of Gaudergrat ridge - periodic boundaries, 9 km² area.

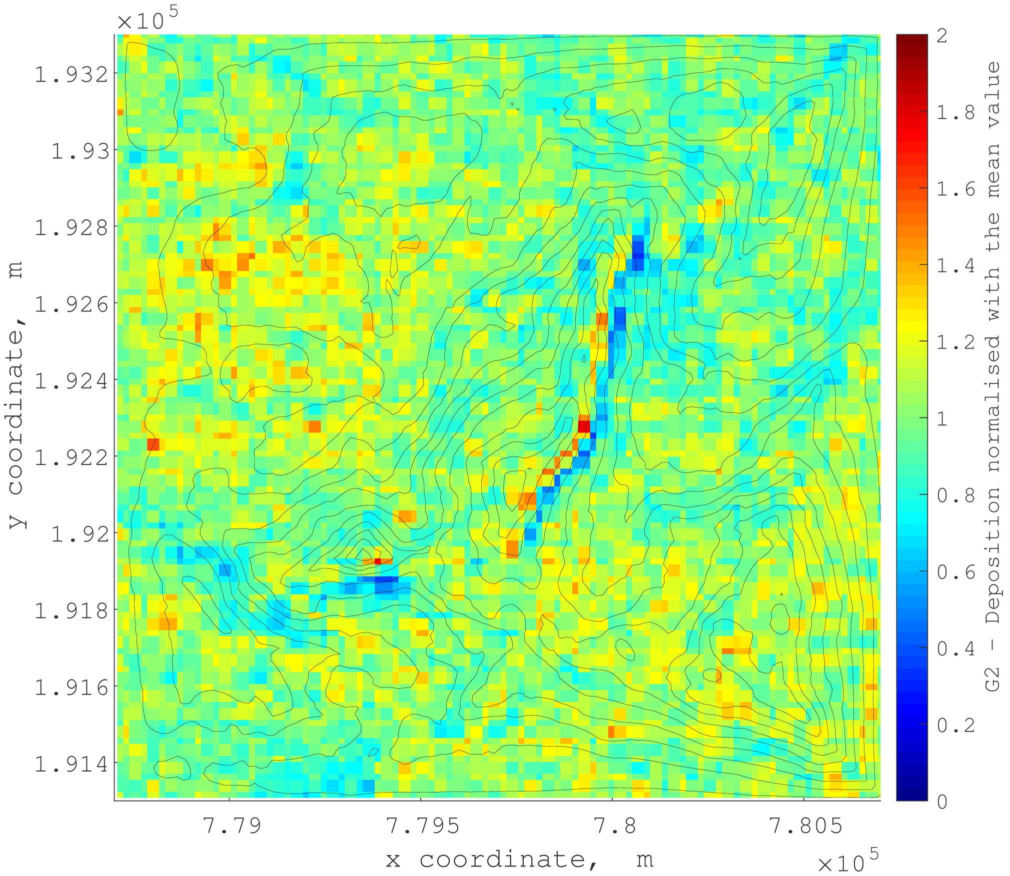

Figure 5.7: Deposition patterns of the 9 km² DTM, clipped on the 4 km² area around the Gaudergrat ridge. Black lines match same elevation points.

- E3: *Gaudergrat3*
  The region shown in Figure 5.8 consists of a 16 km² square area with a computational grid resolution of 31.25² m² and a maximum elevation gain of around 1000 m. The wind direction in the area is still coarsely perpendicular to the steepest part of Gaudergrat's ridge and in this case the simulated velocity field intensity is not much higher than 6 m/s. This is probably due to our underestimation of pressure forcing factor (Π_1 from Equation (2.1a)) while scaling the domain size.

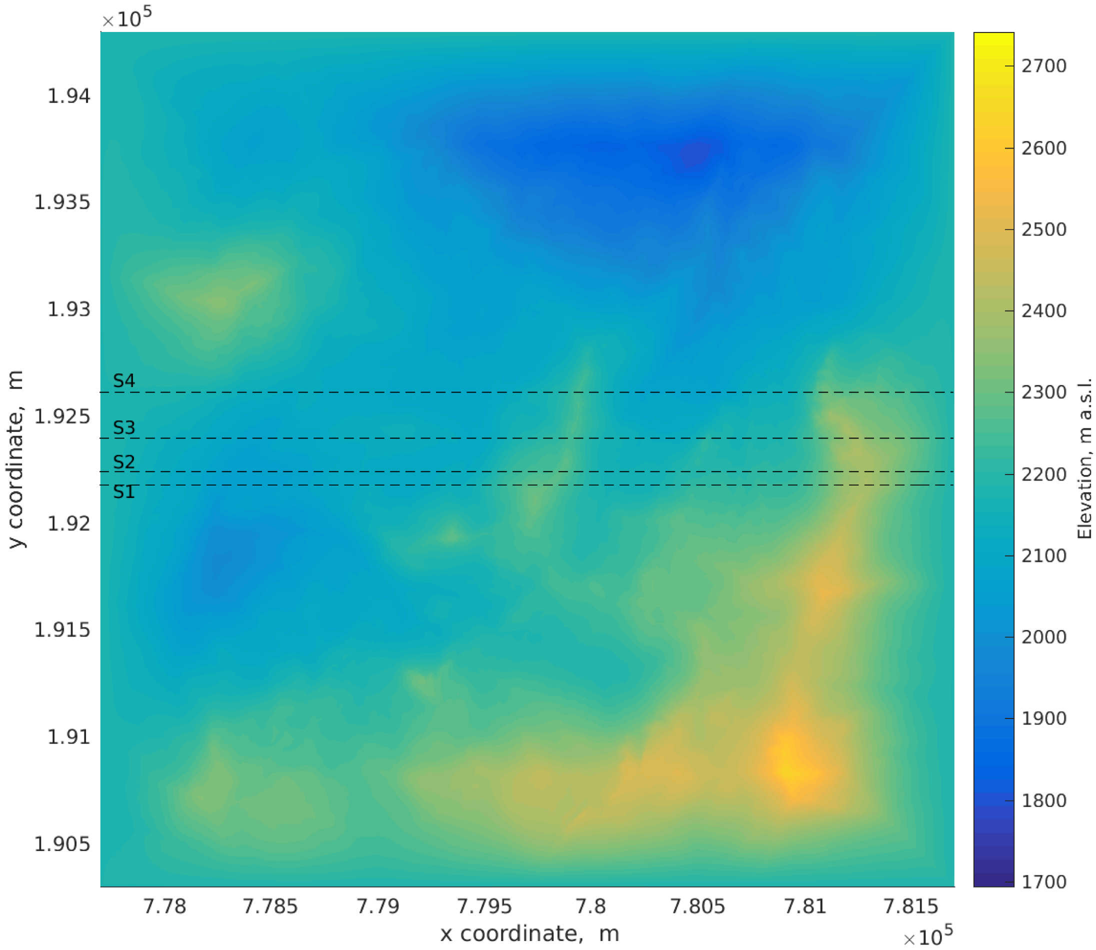

Figure 5.8: Digital Terrain Model of Gaudergrat ridge - periodic boundaries, 16 km² area.

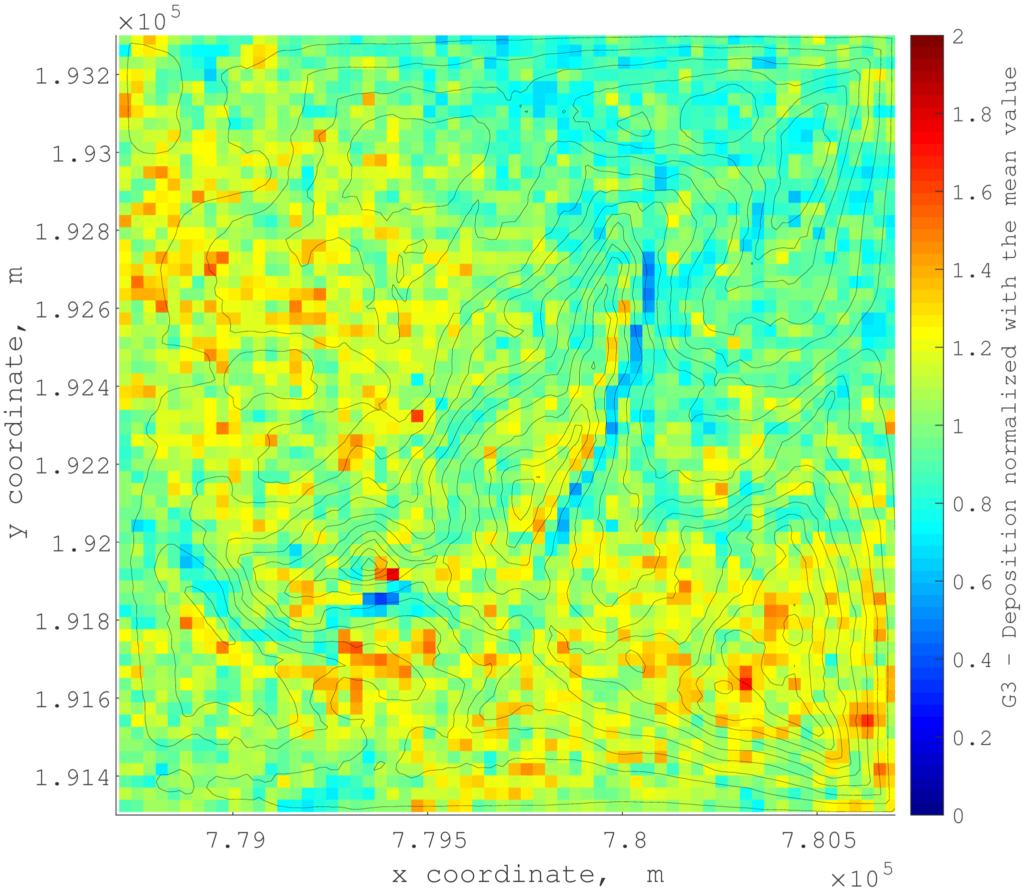

Figure 5.9: Deposition patterns of the 16 km² DTM, clipped on the 4 km² area around the Gaudergrat ridge. Black lines match same elevation points.

What clearly appears after these three different simulations is that the deposition patterns (Figure 5.5, Figure 5.7 and Figure 5.9) are overall very similar to each other. Crossing the Gaudergrat ridge perpendicularly, we can in fact, always observe the alternation: medium deposition in the windward area, maximum accumulation in proximity of the topographic peak and a minimum depisition zone on the lee slope. On the flatter areas upwind and downwind of the ridge, the deposition pattern does not show remarkable patterns.
Please note that, in order to compare sensitivity to domain results, the original Gaudergrat2 and Gaudergrat3 domains have been clipped on the Gaudergrat1 size and this is the reason for spatial resolution differences (Table 4.1).

In order to compare deposition and velocity field among these three settings, we report snow depth profiles and corresponding velocity in Figure 5.10, Figure 5.12 and Figure 5.14 for the sections (S1), (S3) and (S4) indicated in Figure 5.4. Figure 5.11, Figure 5.13 and Figure 5.15 overlay the qualitative snow depth profile predicted in Simulations E1, E2 and E3.

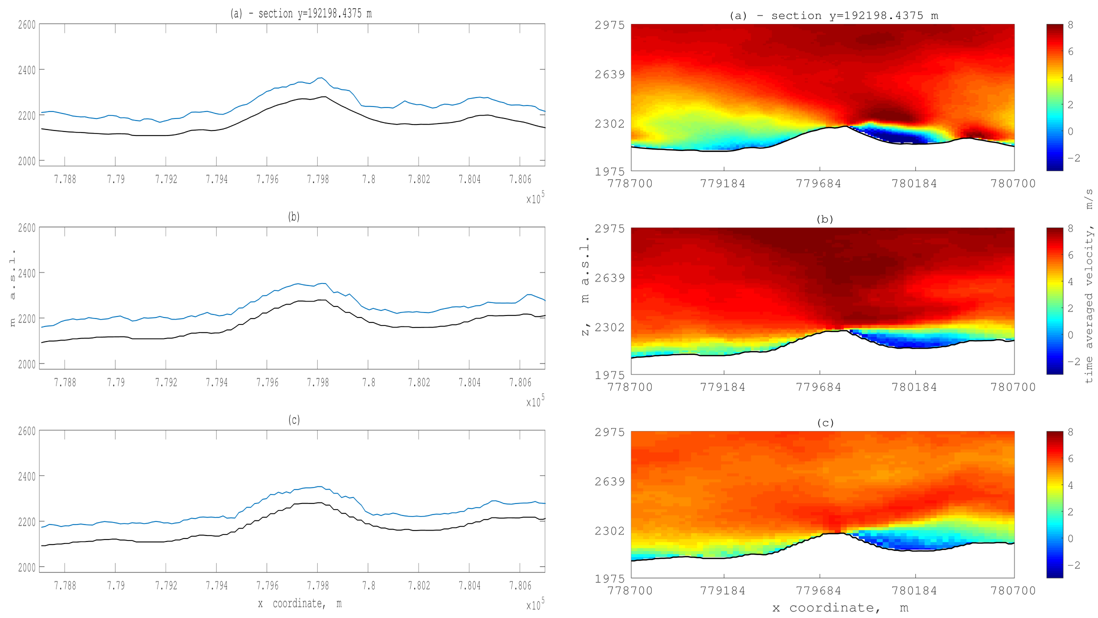

Figure 5.10: (left)Profile geometry changing with DTM, topped by qualitative representation of the snow depth profile (exaggerated height). (right) Total velocity time averaged. a) Gaudergrat1, b) Gaudergrat2 and c) Gaudergrat3. Section (S1).

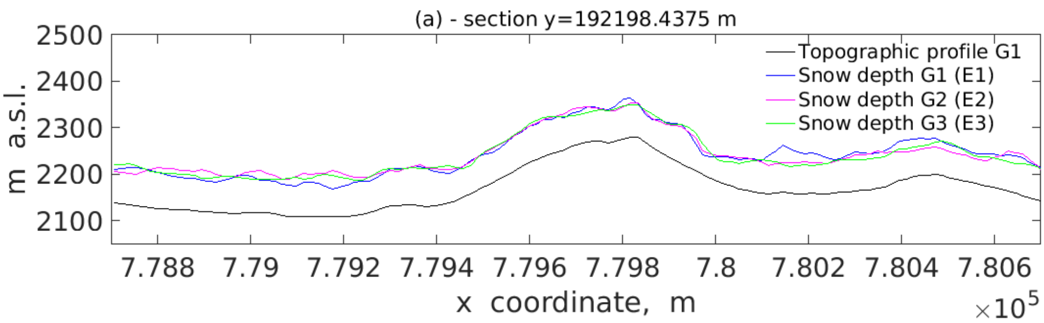

Figure 5.11: Predicted snow depth in simulations E1, E2 and E3, showed (in an exaggerated scale) on the topographic profile G1. Section (S1).

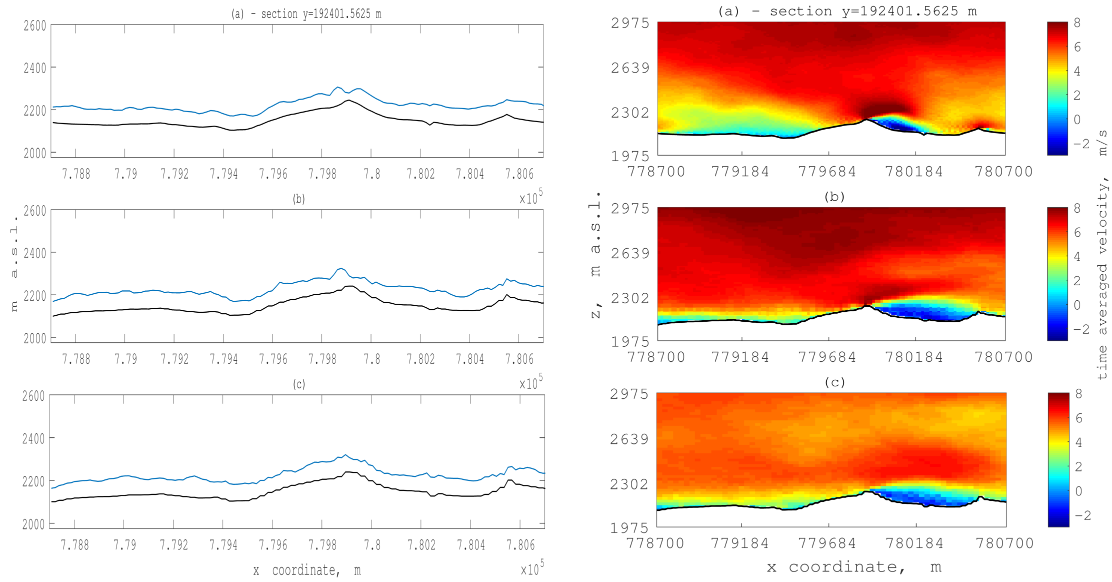

Figure 5.12: (left)Profile geometry changing with DTM, topped by qualitative representation of the snow depth profile (exaggerated height). (right) Total velocity time averaged. a) Gaudergrat1, b) Gaudergrat2 and c) Gaudergrat3. Section (S3).

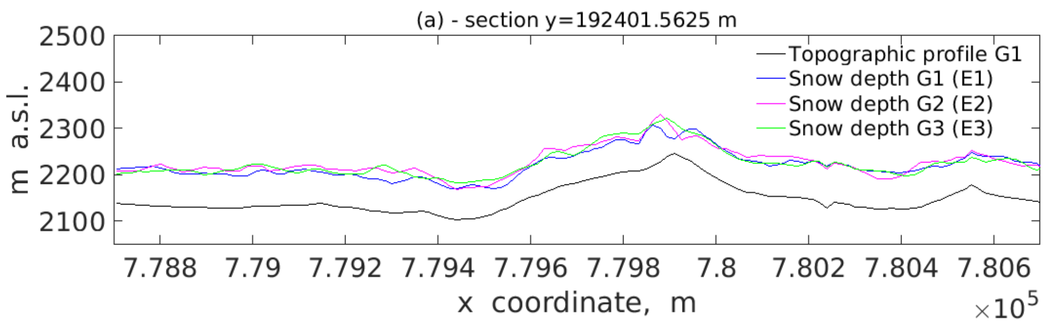

Figure 5.13: Predicted snow depth in simulations E1, E2 and E3, showed (in an exaggerated scale) on the topographic profile G1. Section (S3).

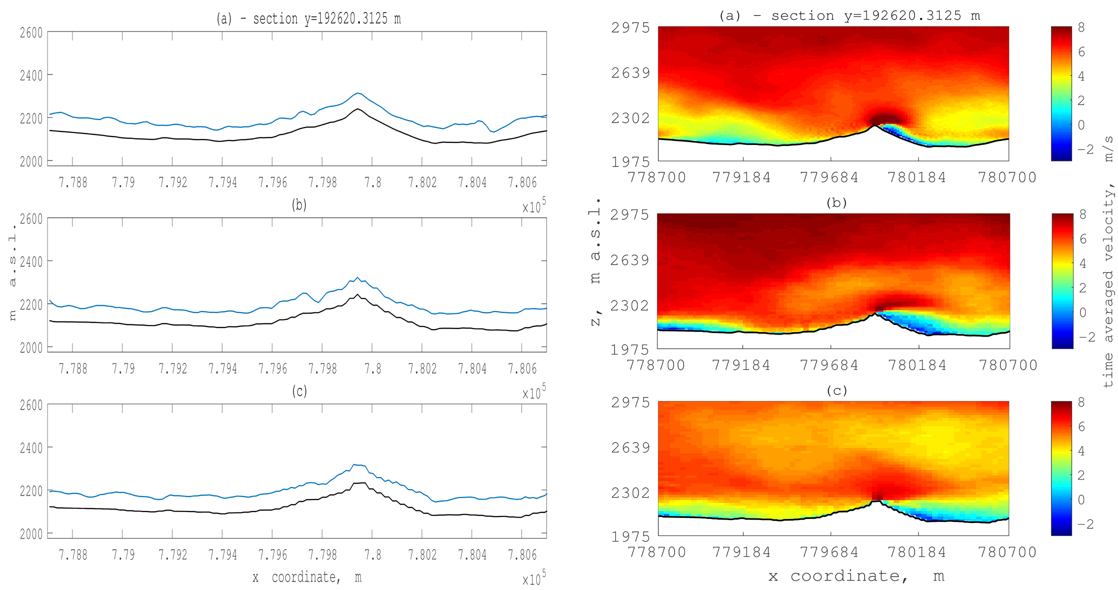

Figure 5.14: (left)Profile geometry changing with DTM, topped by qualitative representation of the snow depth profile (exaggerated height). (right) Total velocity time averaged. a) Gaudergrat1, b) Gaudergrat2 and c) Gaudergrat3. Section S4

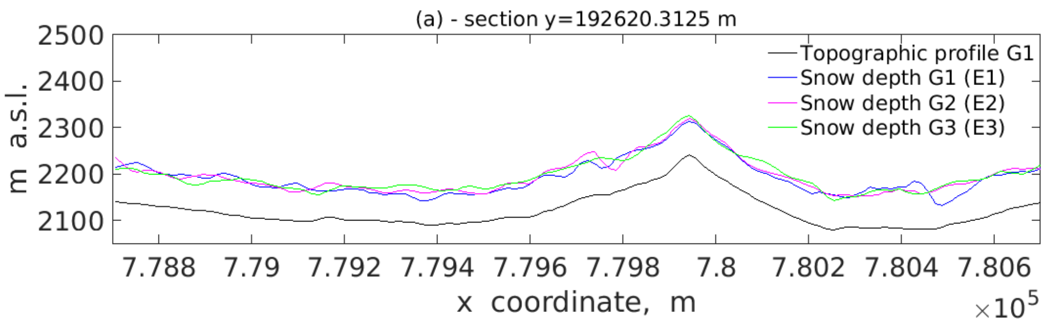

Figure 5.15: Predicted snow depth in simulations E1, E2 and E3, showed (in an exaggerated scale) on the topographic profile G1. Section (S4).

Looking at highest and steepest points that we can find in each section, we can comment snow accumulation features.

In the southern section (S1), identified by y = 192198.4375 m (Figure 5.10), which is not characterized by a sharp topographic peak, we observe a clear zone of accumulation on the summit, a point of decrease immediately after and then, again, an accumulation zone followed by a bump in the mid descendent slope before the snow accumulation becomes more regular in the valley below.

In the northern section (S3) (Figure 5.12) the snow profile appears less homogeneous across the ridge. Plots (a) and (b) show a maximum accumulation before the peak, a minimum

exactly on the hilltop and then again an accumulation zone. In this section, the low deposition zone in the middle of the lee slope is less evident than in (S1) and the maximum accumulation shifted.
In the northern most section (S4), which is the sharpest among the three shown, the snow depth trend (Figure 5.14) does not present particularly strong variations around the hilltop. The snow cover follows the shape of the crest, with a deposition maximum slightly shifted after the peak. A local minimum is visible in the mid windward slope before the peak.

Differences in position of deposition maxima and minima across the ridge, among the three showed sections, are due to local topographical features and wind flow characteristics. As said, the complex topography, with its valleys, peaks and variable steepness, generates vorticity, flow convergence or divergence different in each location. The small differences among a) b) or c) plots (G1, G2 and G3) in each section are due to the different domain sizes and spatial resolutions, which produce slightly different flow conditions around the ridge (Figure 5.10, Figure 5.12,Figure 5.14).

Differences in velocity field intensity, mainly visible in the *Gaudergrat3* for a weaker field, can be due, again, to the different domain size and flow settings we had to fix for each simulation.

To have a direct comparison of the snow depositions simulated for the different domain resolutions, we can also look at Figure 5.11, Figure 5.13 and Figure 5.15 where the three different snow depths are reported (always in an exaggerated vertical axis) on the topography with highest resolution, i.e. the one with the smallest domain size.
To conclude this sensitivity analysis on the domain size and boundary modification, we can firstly observe that, in terms of deposition patterns the expectations were confirmed by the modelled deposition across the central diagonal ridge. These observations motivate us to adopt the smaller domain (E1, *Gaudergrat1*) for the following analyses, to take advantage of the higher spatial resolution and perform more accurate simulations of turbulent motions and particle trajectories.

5.2 Sensitivity to velocity field variation

The wind flow interacting with the surface is the main responsible for preferential deposition. In order to fulfil the main goal of this study, we investigate how flow intensity variation affects the snow deposition pattern on the ridge. In particular, we consider simulation E1 as the reference case and perform two additional simulations on the same topography, applying multiplication factors equal to 0.5 (simulation E4) and 2 (simulation E5) (Table 4.2). This procedure modifies uniformly the wind velocity while keeping constant the wind direction.

In E1 the free stream velocity is around 7.38 m/s, in E4 it is around 3.76 m/s while in E5 it is around 14.62 m/s. The durations of all simulations is approximately 14 minutes. (vd.4.2).

The vector plot of the near-surface velocity field (Figure 5.16), indicates that the flow direction around the ridge is roughly perpendicular to it, which corresponds to the natural conditions described in [Lehning et al., 2008].

For each of these cases (E1, E4, E5) we show the 2D map of the wind field (Figure 5.16 [1]), the resulting 2D deposition map (Figure 5.17, Figure 5.19, Figure 5.21), a vertical section of the flow field (S2) and a vertical section of the snow height distribution (Figure 5.18, Figure 5.20, Figure 5.22). The velocity field that we see displayed (Figure 5.18, Figure 5.20, Figure 5.22) with a color range from blue (-4 m/s) to red (maximum 15 m/s), is the velocity magnitude averaged in time and the y direction. The (a) plots represent vertical sections of the time-averaged velocity field. Plots (b) show how snow deposits on the ridge according to the steepness and the wind direction and intensity. In plots (c) values larger than 1 indicate deposition larger than the mean, smaller values otherwise. In order to prove the 45° wind direction we additionally show an x wise vertical section and the y wise section which intersects the highest point of the x wise topographic profile(Figure 5.18).
We then go more into the details of the various physical flow characteristics contributing to the final deposition. For this purpose we only focus on sections (S1) and (S4), the most south and north ones (see from Figure 5.27 to Figure 5.35). We recall what said in Section 2.5: the flow-particle interplay can be controlled by St and Fr^2. Where St expresses the ratio between inertia and advection and Fr^2 expresses the ratio between inertial and gravitational forces.

[1] The vectorial representation of the flow does not change among E4 and E5 except for arrows length (intensity)

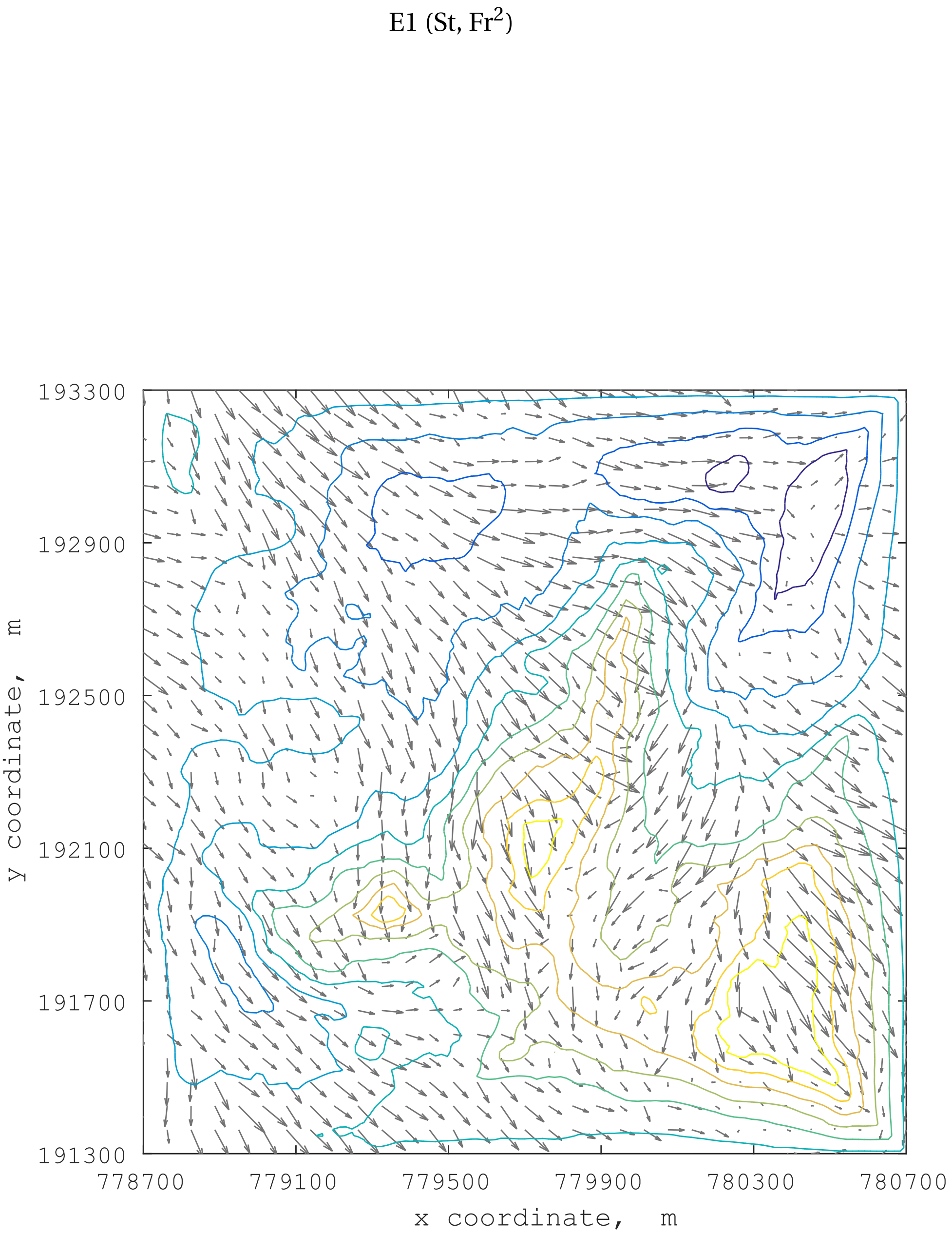

Figure 5.16: Instantaneous wind field - reference case E1. Arrows are proportional to the flow intensity. In colors iso-elevation lines.

Given the slightly different durations of the simulations, deposition values are always normalised (divided for the mean deposition value on the area). The vector field of the near-surface wind flow indicates that the wind velocity and direction have a visible effect on the deposition pattern.

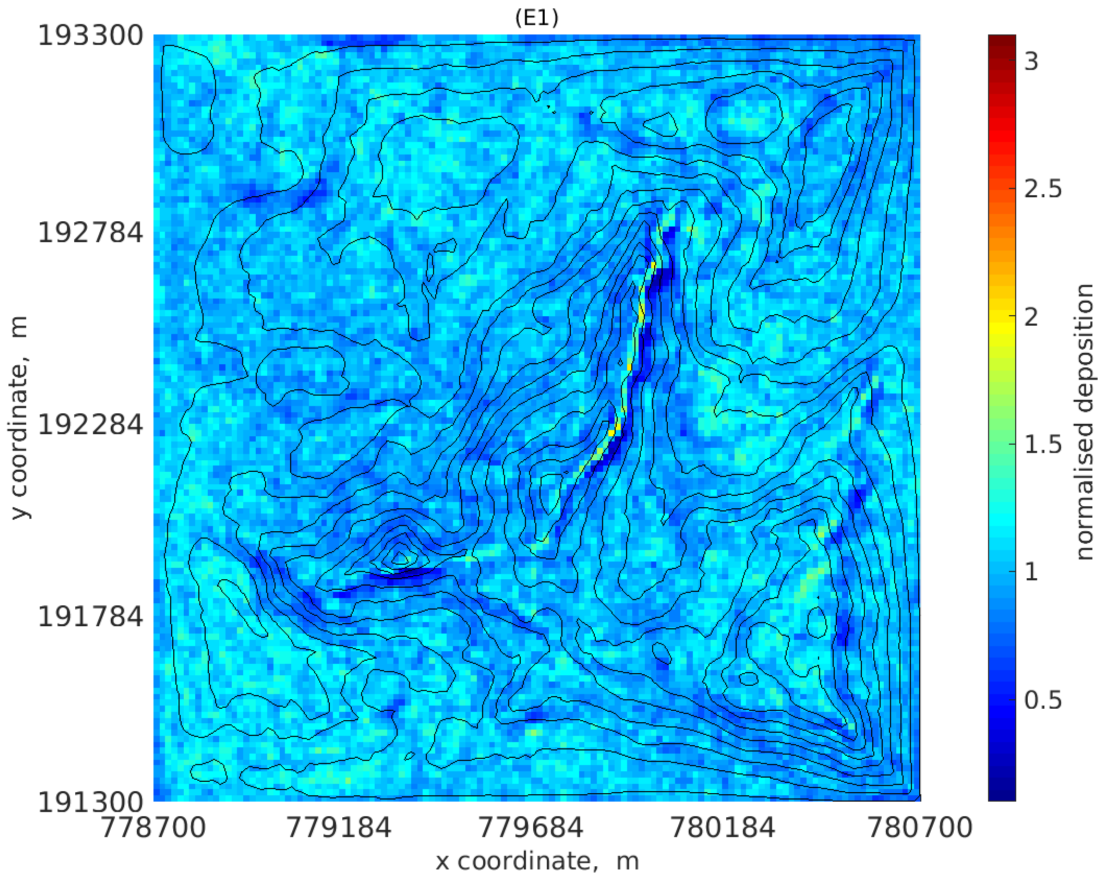

Figure 5.17: Normalised deposition and (height) contour lines - reference case E1.

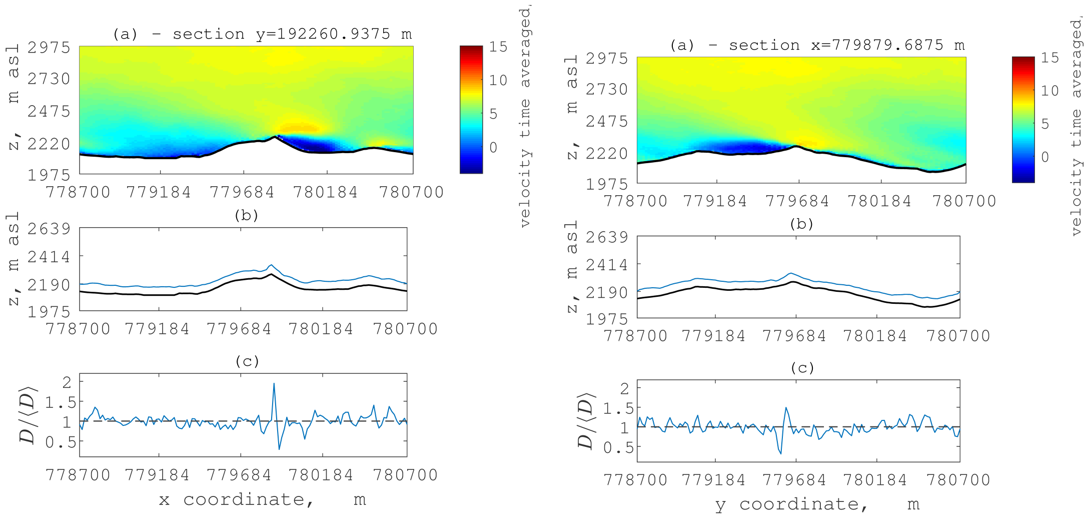

Figure 5.18: a)Vertical section of time and y or x averaged total wind intensity (m/s); b)topographic profile topped by the qualitative snow depth profile (magnified height); c) decreased or increased deposition with respect to the normalised value. Reference case E1. (left) Geographic xz section (S2). (right) yz section crossing the topographic peak in (S2).

E4 0.5(St, Fr^2)

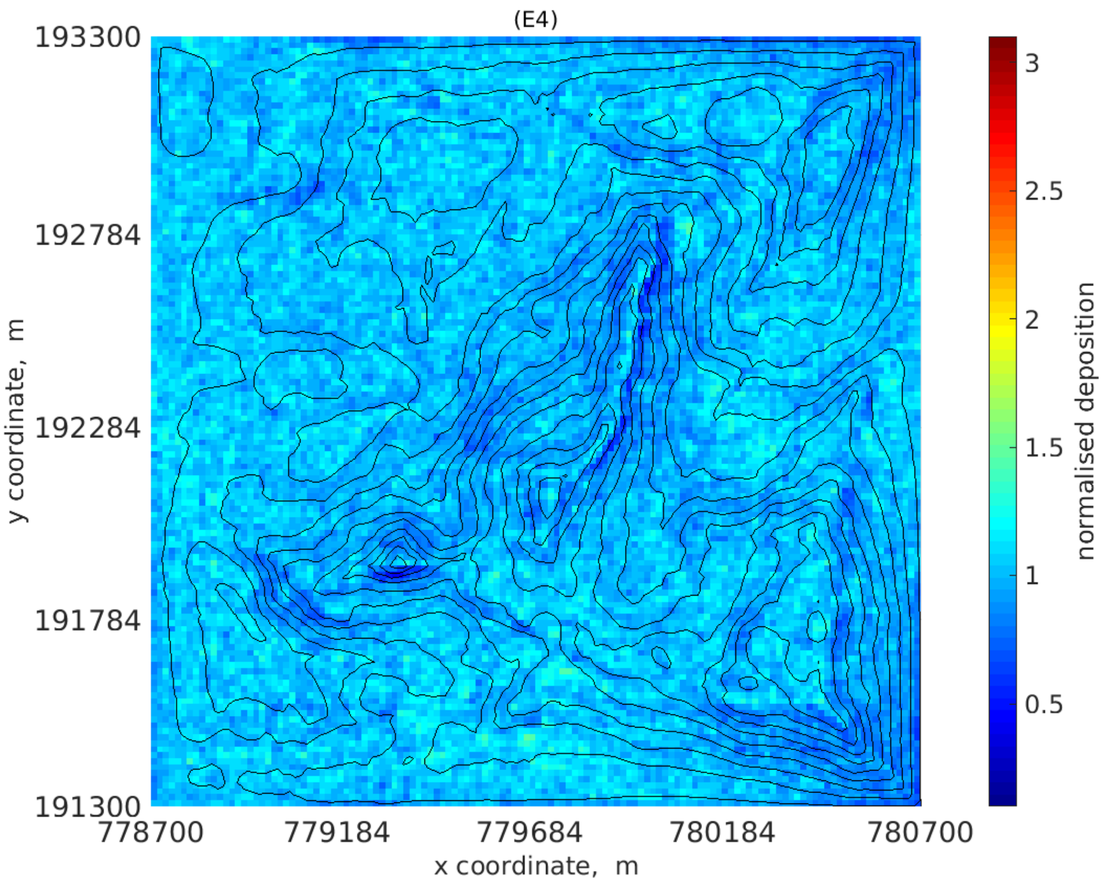

Figure 5.19: Normalised deposition and (height) contour lines. Scaled velocity, simulation E4.

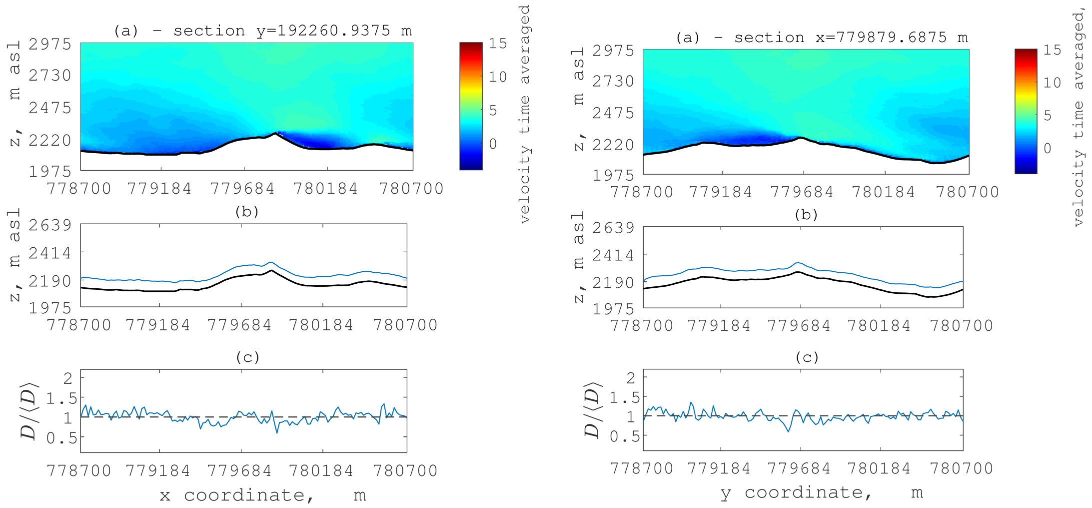

Figure 5.20: a)Vertical section of time and y or x averaged total wind intensity (m/s); b)topographic profile topped by the qualitative snow depth profile (magnified height); c) decreased or increased deposition with respect to the normalised value. Scaled wind field, E4. (left) Geographic xz section (S2). (right) yz section crossing the topographic peak in (S2).

E5 2(St, Fr^2)

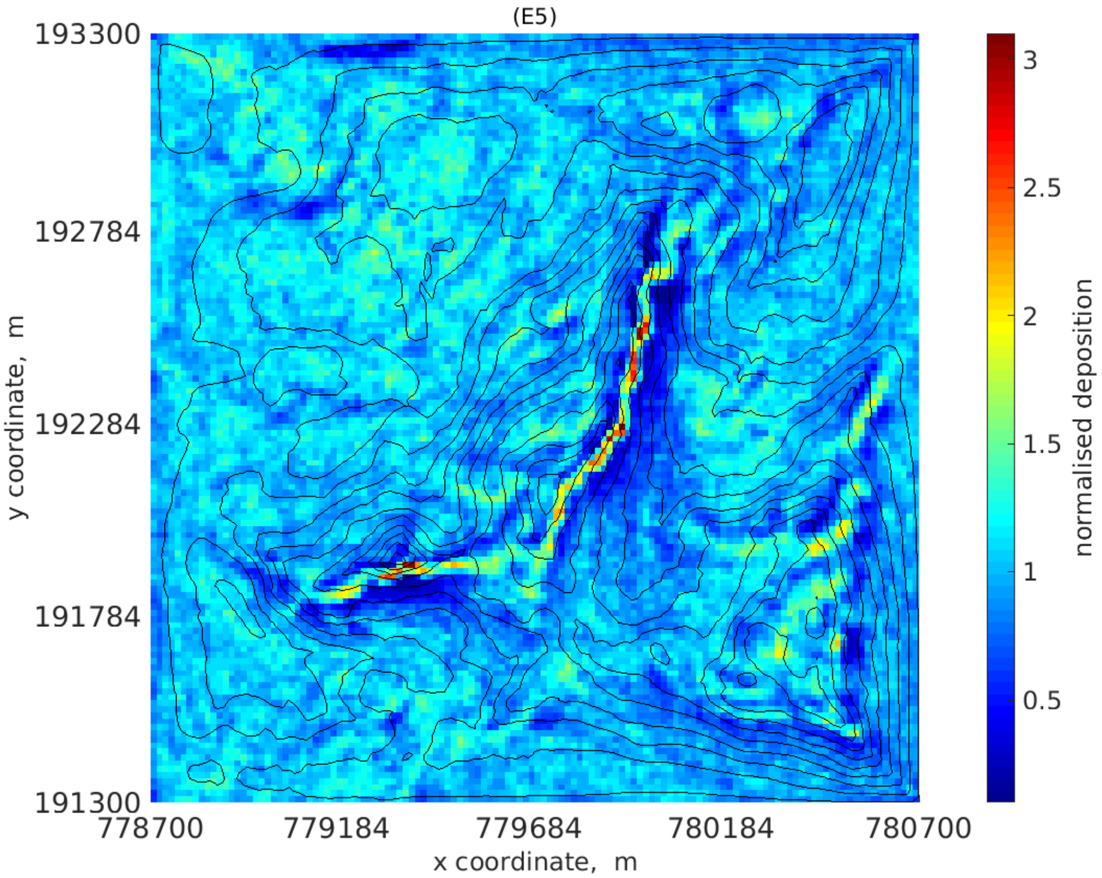

Figure 5.21: Normalised deposition and (height) contour lines. Doubled velocity, simulation E5.

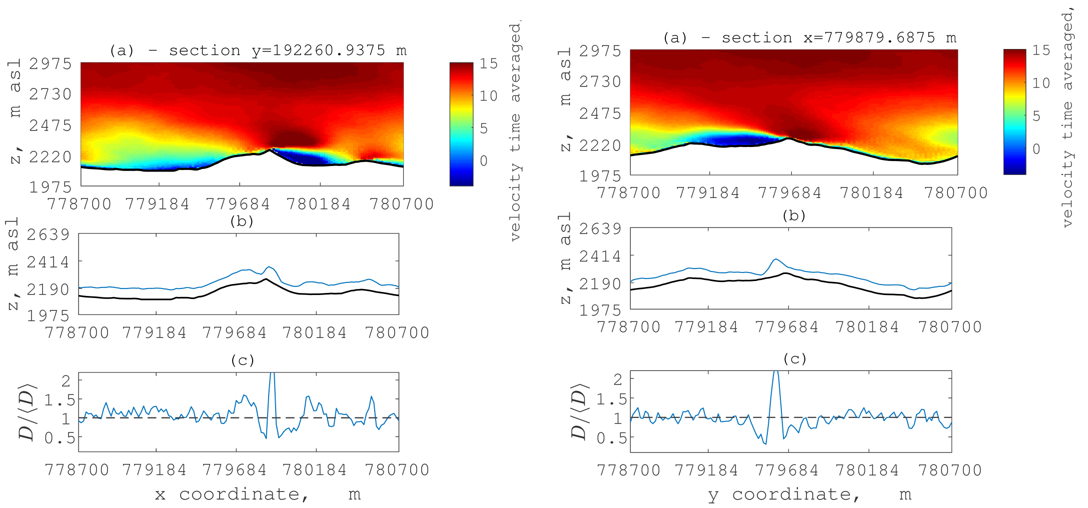

Figure 5.22: a)Vertical section of time and y or x averaged total wind intensity (m/s); b)topographic profile topped by the qualitative snow depth profile (magnified height); c) decreased or increased deposition with respect to the normalised value. Doubled wind field, E5. (left) Geographic xz section (S2). (right) yz section crossing the topographic peak in (S2).

Observing the three different set-up outputs, from Figure 5.17 to Figure 5.22, it is clear that snow deposition patterns depend on the wind velocity: the peak in accumulation moves from above to immediately after the ridge summit, typically preceded and followed by a zone of small deposition. The steeper is the ridge, the more variable the deposition is. Progressing from case E1 to E5, we also see that the stronger the wind field, the more variable the snow depth profile. The deposition maxima and minima become more intense and localised in the E5 case; in other words increasing the wind field intensity, the peak in accumulation becomes clearly visible after the crest; this is located between the minimum deposition on the summit and the subsequent deposition minimum which interests a larger zone on the leeward side (Figure 5.22). Therefore, a stronger near-surface wind field enhances preferential deposition by increasing the effect of flow advection on particle dynamics. Because considering a xz section or yz section does not make much difference in terms of wind field and snow deposition, for simplicity, we will show only xz sections (as indicated in Figure 5.4) from now on.

To provide a better understanding of the main factors influencing the snowflake deposition (Figure 5.17, Figure 5.19 and Figure 5.21) we compare the three settings taking the same topographic sections ((S1) and(S4) from Figure 5.4). We show for them the sub-grid scale contribution to the kinetic energy of the flow (Figure 5.23), the LES resolved stress (Figure 5.24), the deposition profiles (Figure 5.27) associated to the wind intensity, the directions of the flow and mass flux (Figure 5.28), the vertical velocity (Figure 5.29) and vertical mass flux (Figure 5.34). Comparing the just mentioned graphs it appears more evident the effect of wind intensity on precipitation distribution.

The sub-grid scale component of turbulent kinetic energy (Figure 5.23a and Figure 5.25a) shows higher values in a zone which develops along the stream wise direction from the crest, above the flow recirculation zone in the E4 case, where the transition from recirculation zone (negative velocity) to the positive undisturbed mean flux is more rapid than in E1 and E5. Resolved turbulent stress (Figure 5.24 and Figure 5.26), given in a normalised form, is higher in the recirculation zone and in mid channel areas before the flow impacts the ridge; moreover it appears to be higher in the E4 simulation (the one with the lowest flux intensity). Although the wind field presents the same behaviour among the different intensities (Figure 5.27 (right) or Figure 5.31 (right)) we can see that higher mean flow implies higher vertical velocity component in the windward side, i.e. a stronger flow updraft which corresponds to a stronger vertical mass flux (Figure 5.34 or Figure 5.34) and particles advection towards the ridge. Increasing Fr^2 (E5), in fact, the correlation between the vertical mass flux and the vertical flow velocity increases [Comola et al., in preparation] because of the loss of control by gravity forces. Looking at Figure 5.28 as well as at Figure 5.32 we observe a total mass flux quite different from the wind flow in the E4 case (plots (a)), that is, enhanced deposition on the windward side, and a nearly flow-parallel total mass flux in the E5 case (plots (c)) which leads snowflakes to deposit preferentially after the mountain peak.

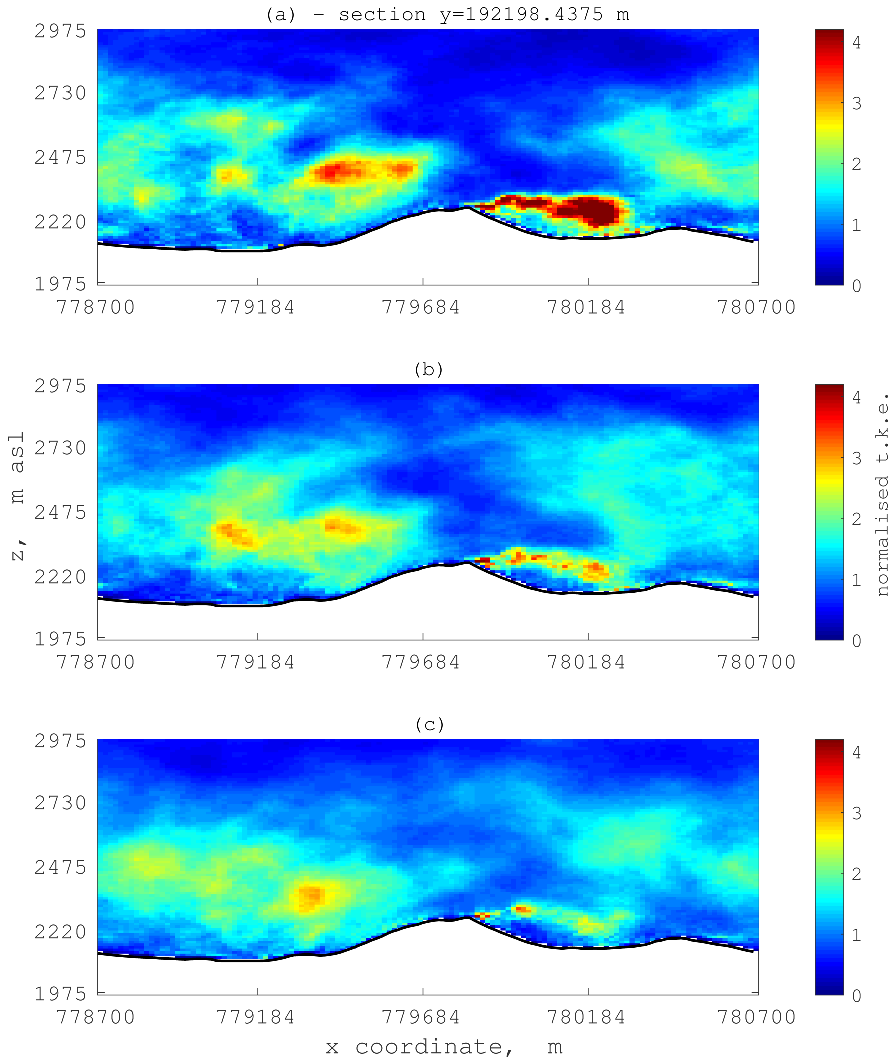

Figure 5.23: Normalised Turbulent Kinetic Energy. Average value on time and y direction. (a) simulation E4, (b) simulation E1, (c) simulation E5. Section (S1)

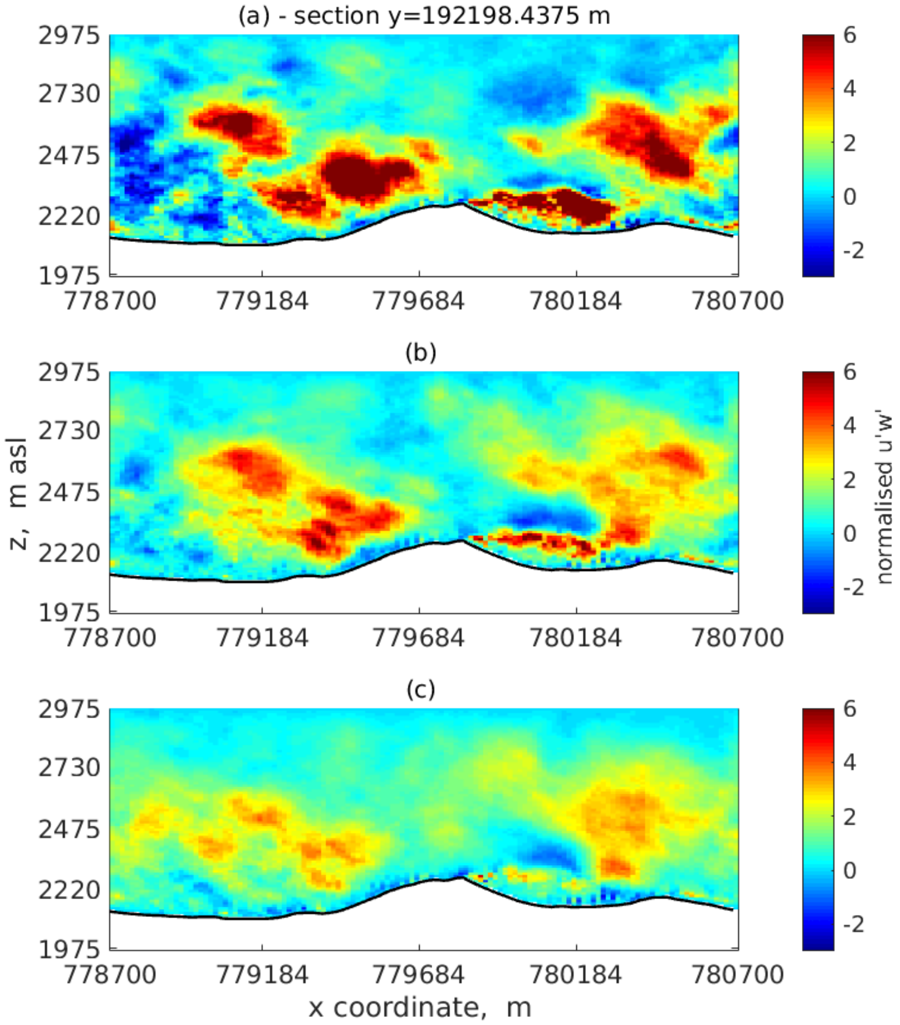

Figure 5.24: Resolved Turbulent Stress, normalised with its mean value. Section (S1), (a) simulation E4, (b) simulation E1, (c) simulation E5.

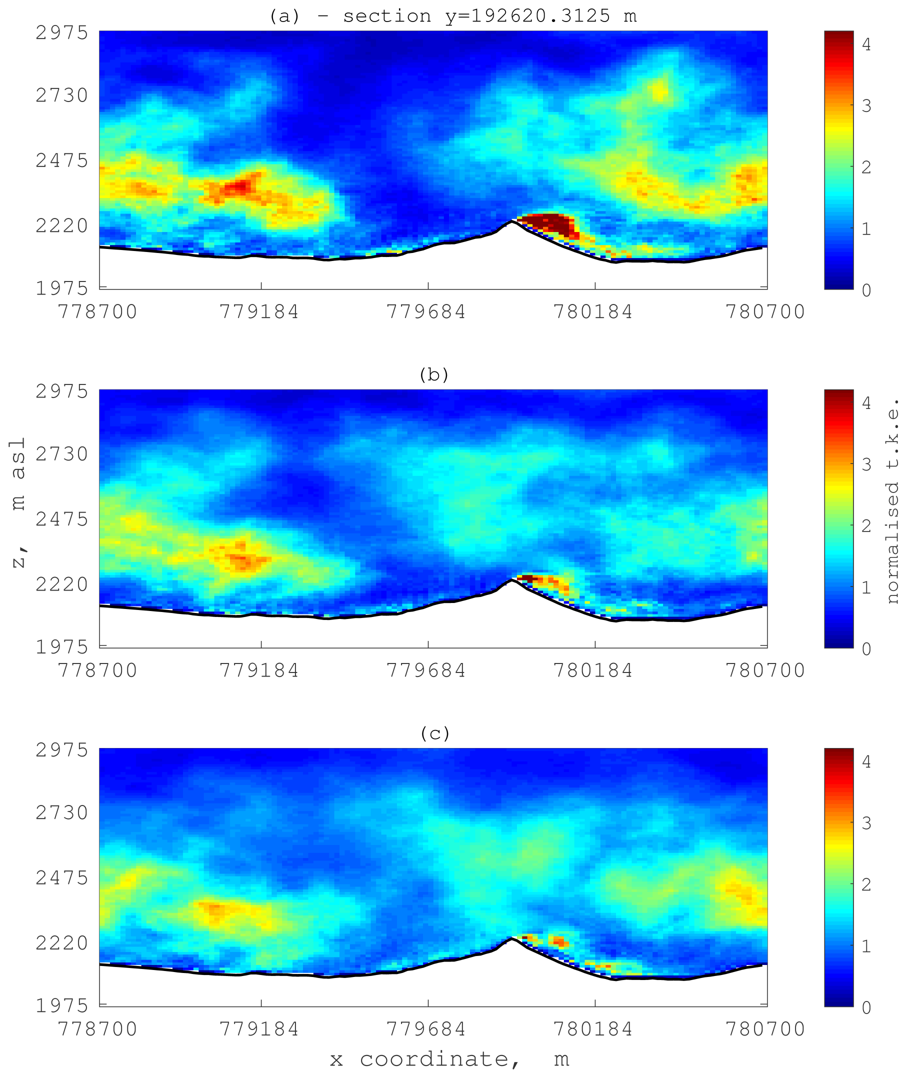

Figure 5.25: Normalised Turbulent Kinetic Energy. Average value on time and y direction. Section (S4), (a) simulation E4, (b) simulation E1, (c) simulation E5.

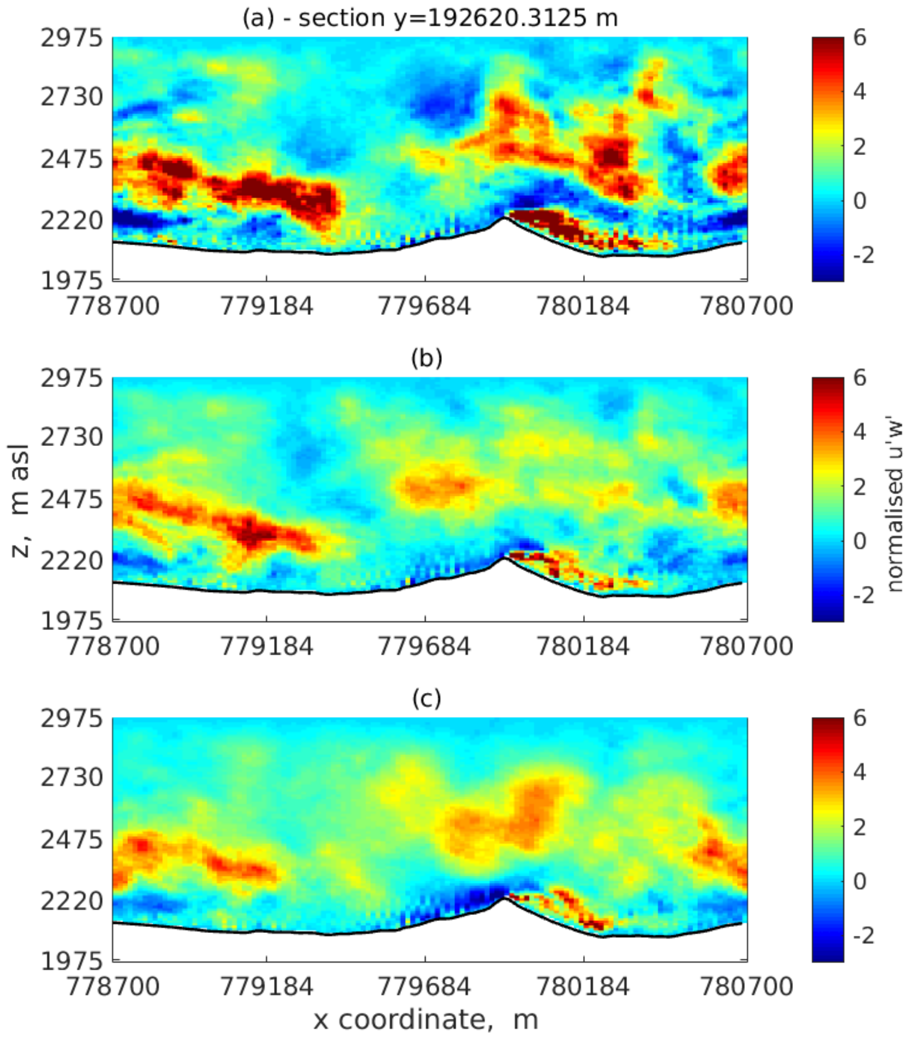

Figure 5.26: Resolved Turbulent Stress, normalised with its mean value. Section (S4), (a) simulation E4, (b) simulation E1, (c) simulation E5.

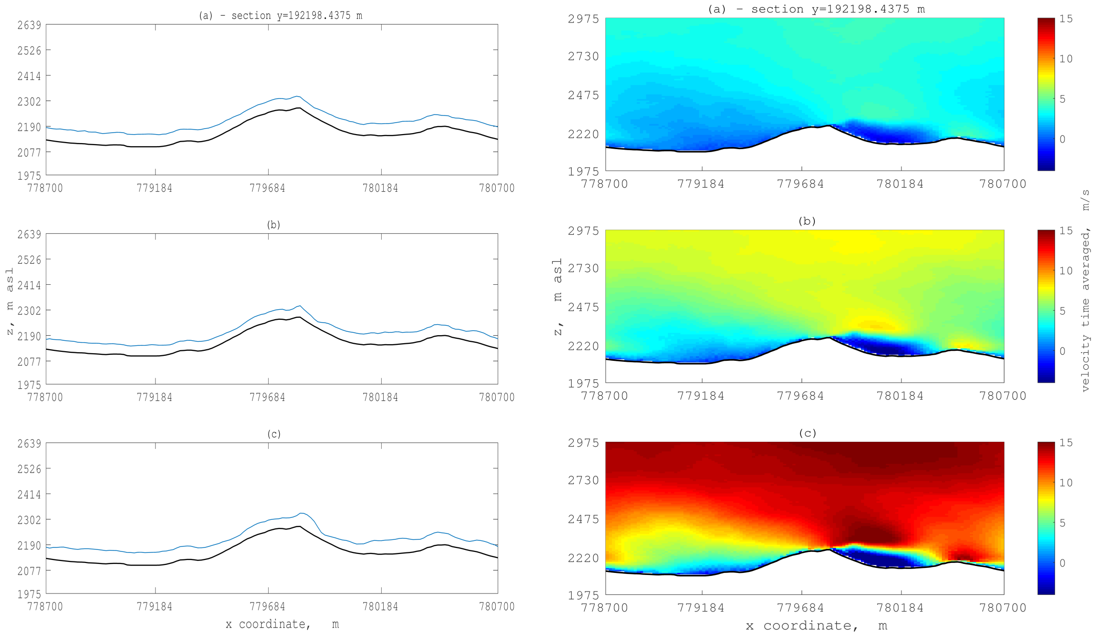

Figure 5.27: (left) Topographic profile topped by the qualitative snow depth profile; (right) vertical section of time and y averaged total wind intensity. Geographic xz section (S1). (a) simulation E4, (b) simulation E1, (c) simulation E5.

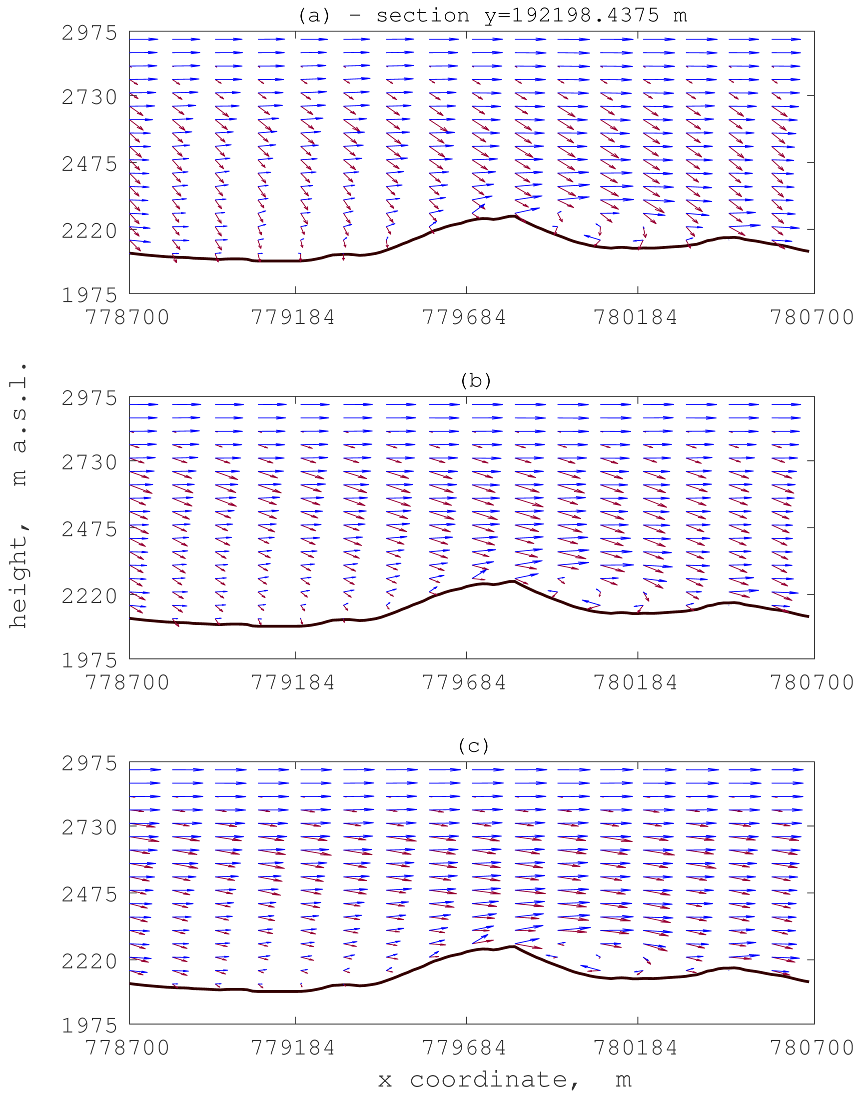

Figure 5.28: Advection versus gravity contribution according to wind field intensity changing. Section (S1). (a) simulation E4, (b) simulation E1, (c) simulation E5.

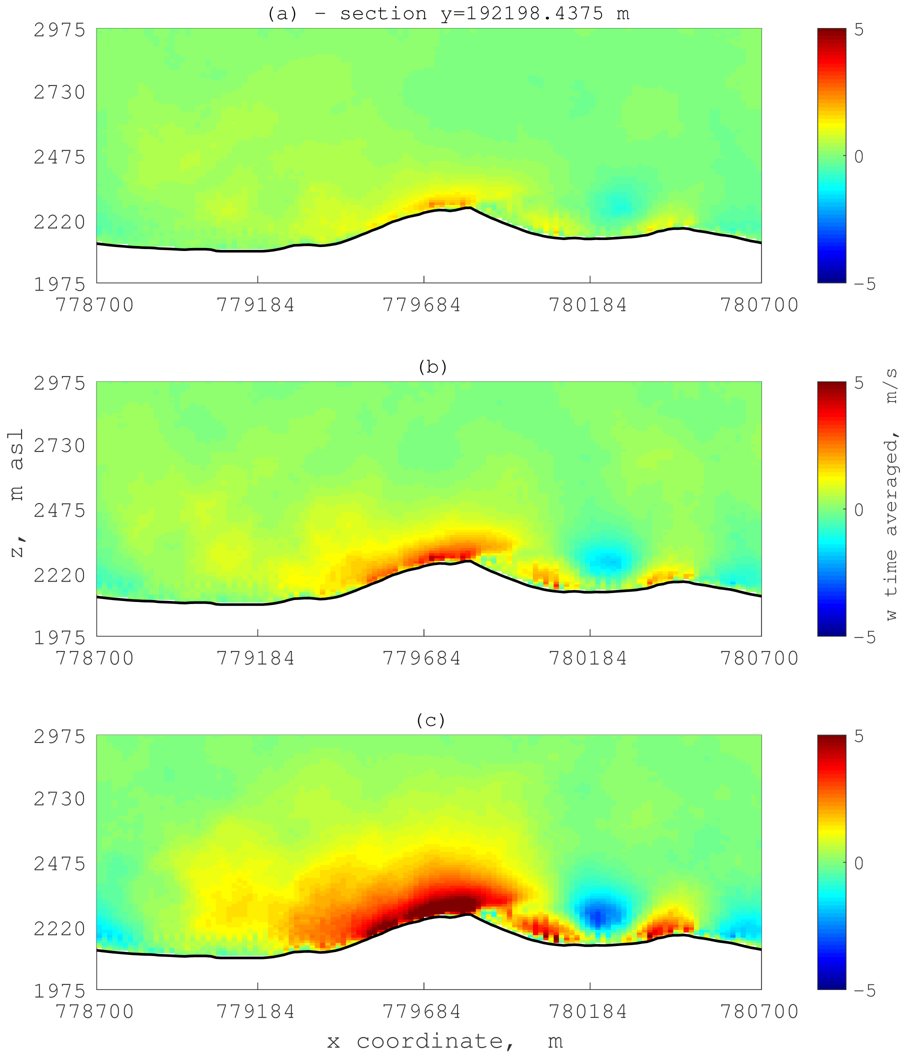

Figure 5.29: Vertical component of the wind velocity. Average value among time and y direction. Section (S1), (a) wind field intensity as in simulation E4, (b) wind field intensity as in simulation E1, (c) wind field intensity as in simulation E5.

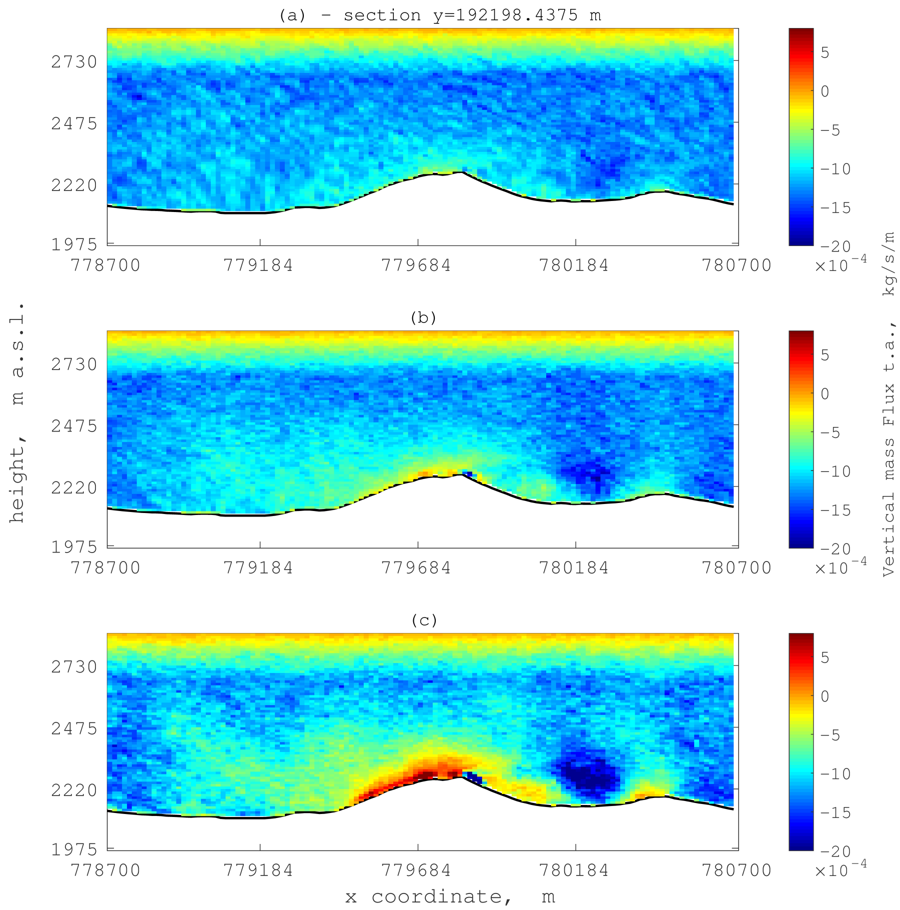

Figure 5.30: Vertical mass flux. Average value on time and y direction. Section (S1), (a) simulation E4, (b) simulation E1, (c) simulation E5.

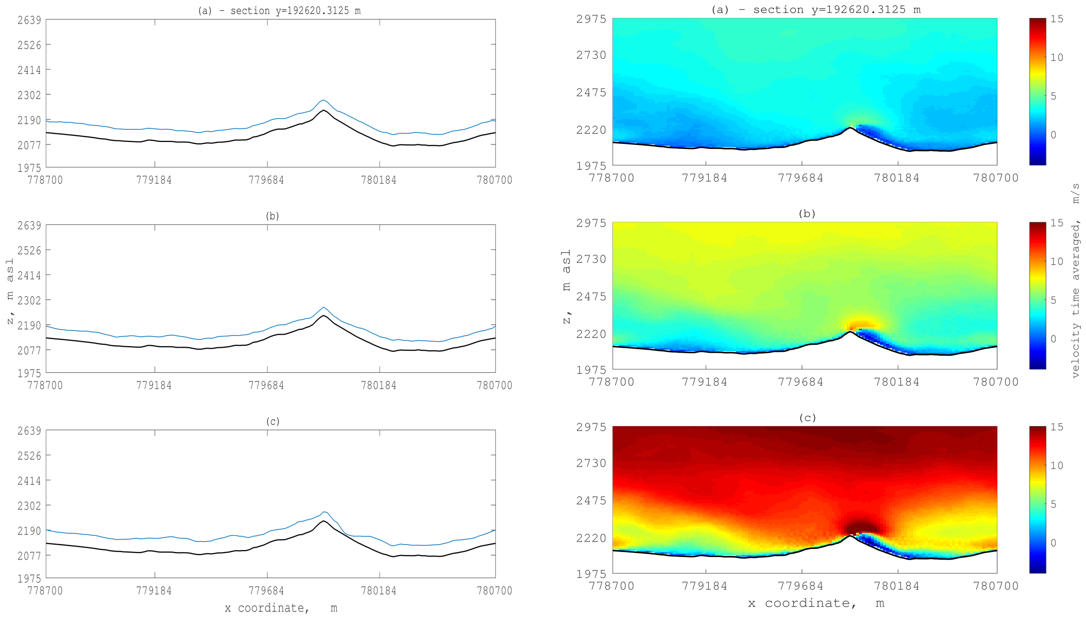

Figure 5.31: (left) Snow deposition (exaggerated respect the ridge height scale), (right) wind mean velocity among time and y direction. Section (S4), (a) wind field intensity as in simulation E4, (b) wind field intensity as in simulation E1, (c) wind field intensity as in simulation E5.

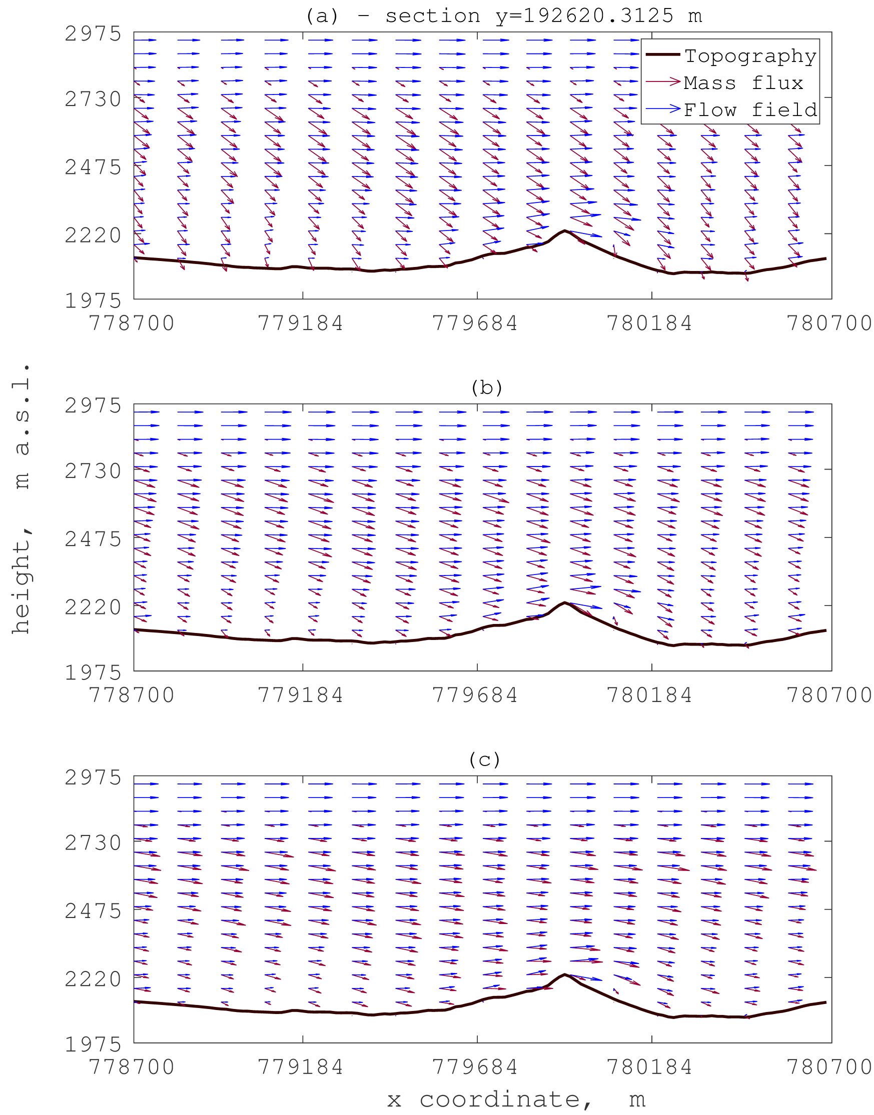

Figure 5.32: Advection versus gravity contribution according to wind field intensity changing. Section (S4), (a) wind field intensity as in simulation E4, (b) wind field intensity as in simulation E1, (c) wind field intensity as in simulation E5.

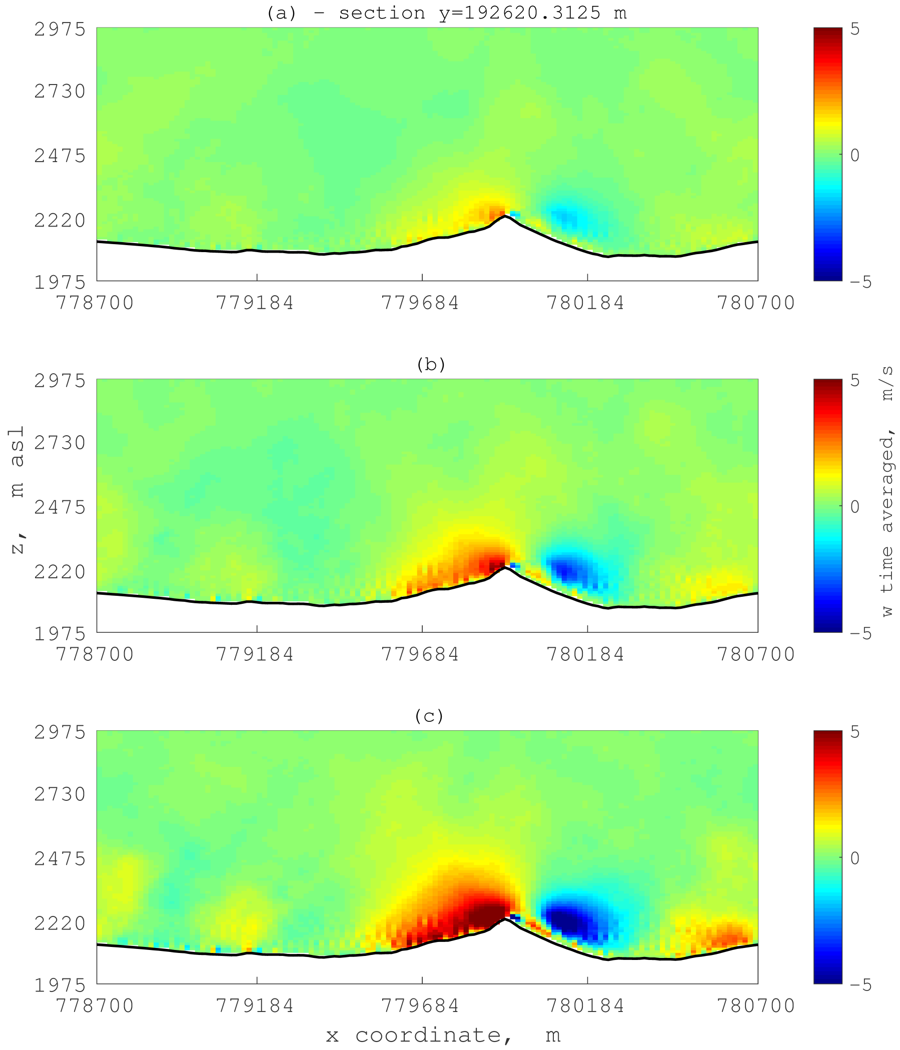

Figure 5.33: Vertical component of the wind velocity, Average value on time and y direction. Section (S4), (a) wind field intensity as in simulation E4, (b) wind field intensity as in simulation E1, (c) wind field intensity as in simulation E5.

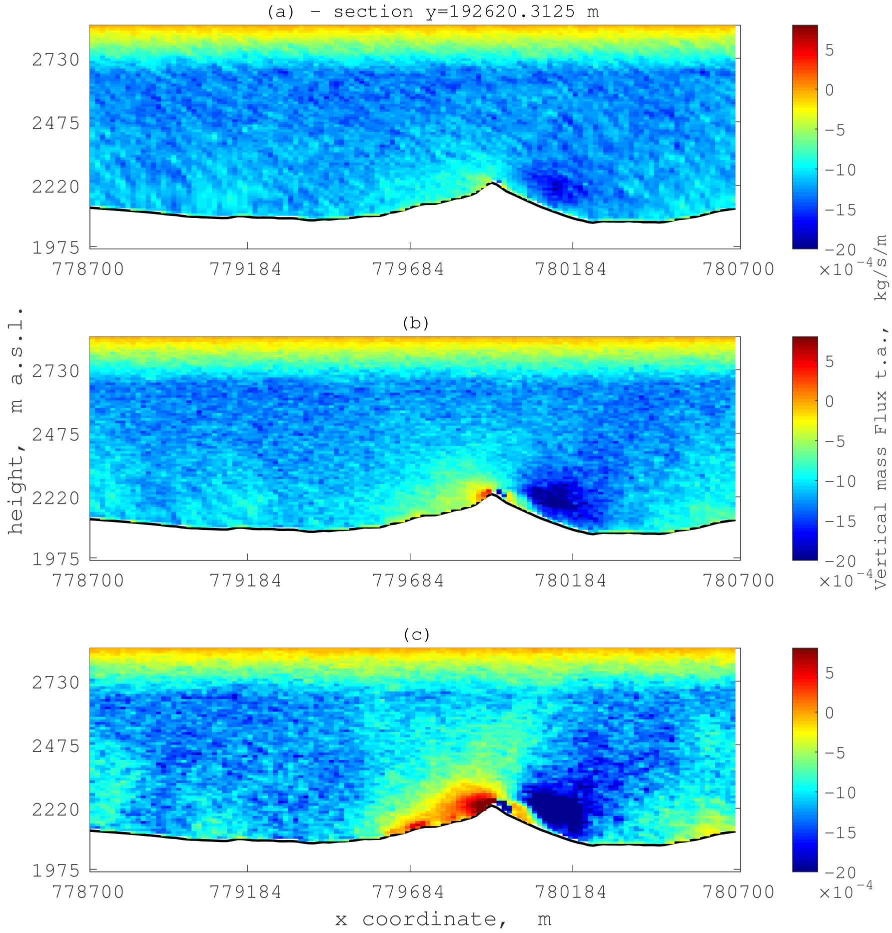

Figure 5.34: Vertical mass flux. Average value on time and y direction. Section (S4), (a) simulation E4, (b) simulation E1, (c) simulation E5.

Finally, looking at Figure 5.35, we can see how increasing wind intensity, changes the deposition above the ridge. The green line, corresponding to the lowest velocity field is the one which most accurately follows the topography among the three; the magenta line (reference velocity) is slightly above the green one on the windward slope and the blue line, corresponding to the highest velocity simulated, has more visible variability, in particular it express quite clearly how preferential leeward deposition occurs creating intense accumulation before and after the peak and low deposition zone on the top and in the upper windward slope.

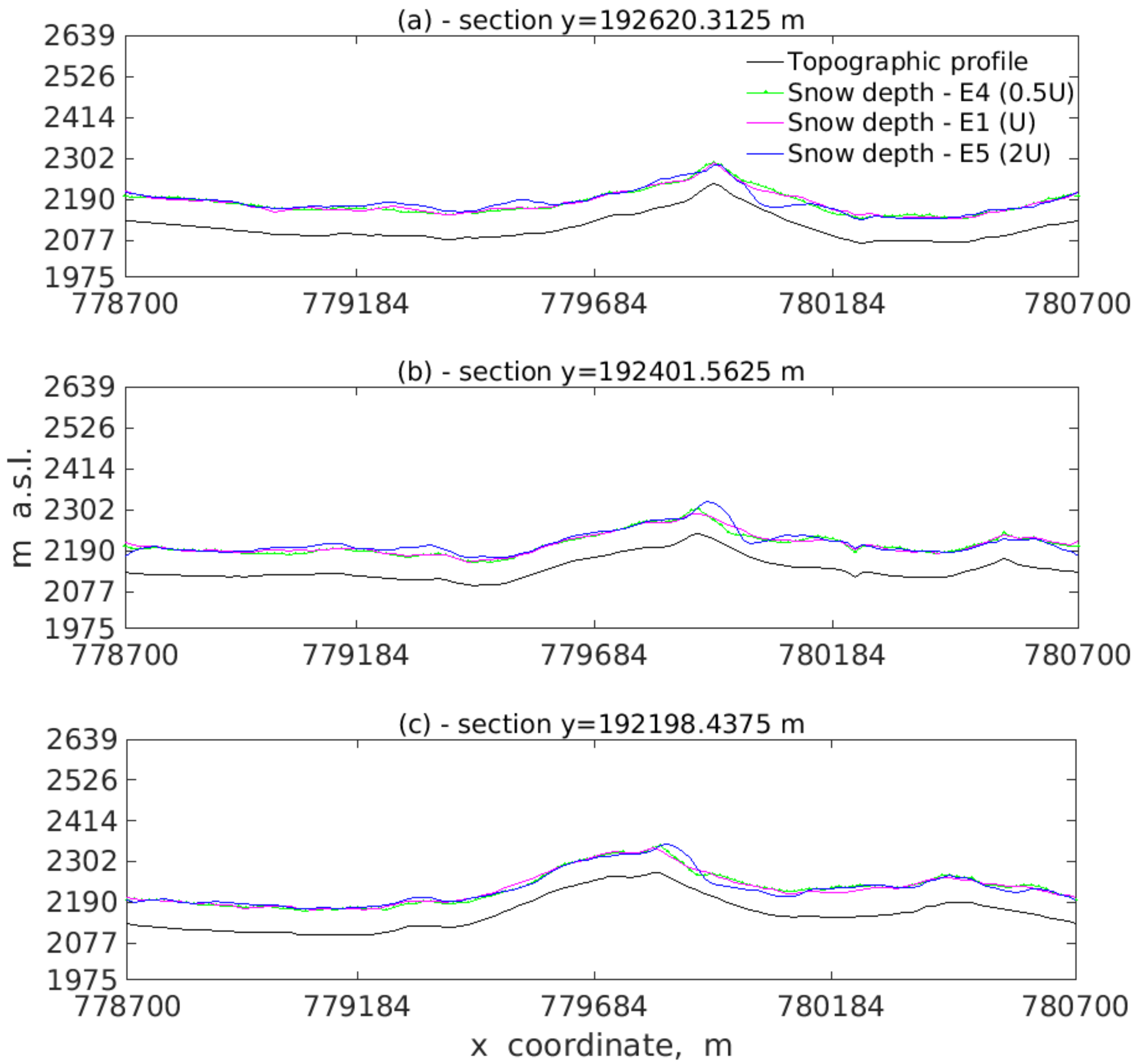

Figure 5.35: Comparison of snow depth variability in the three different settings (E1, E4, E5). (a) Section (S4), (b) Section (S3), (c) Section (S1).

5.3 Particle inertia effect on preferential deposition

We also investigate how much inertia of transported snow particles affects the deposition patterns. In other words, we investigate how the inertialess particles assumption may affect the simulation of snow depth distribution. As mentioned in the introduction, most previous studies of preferential deposition over real topography used a stationary form of the advection diffusion equation that neglects particle inertia (Lehning et al. [2008],Mott et al. [2010]). With our LSM model, we are able to include or exclude the effect of inertia in the particle equation of motion 2.6. The flow field is the same of E1 (Figure 5.16 and Figure 5.18) but particle relaxation time goes to zero: particles react immediately to flow field variations. Precipitation particles are transported by the fluid but they have a downward settling velocity equal to 1 m/s (following previous field observations by [Garrett and Yuter, 2014]).

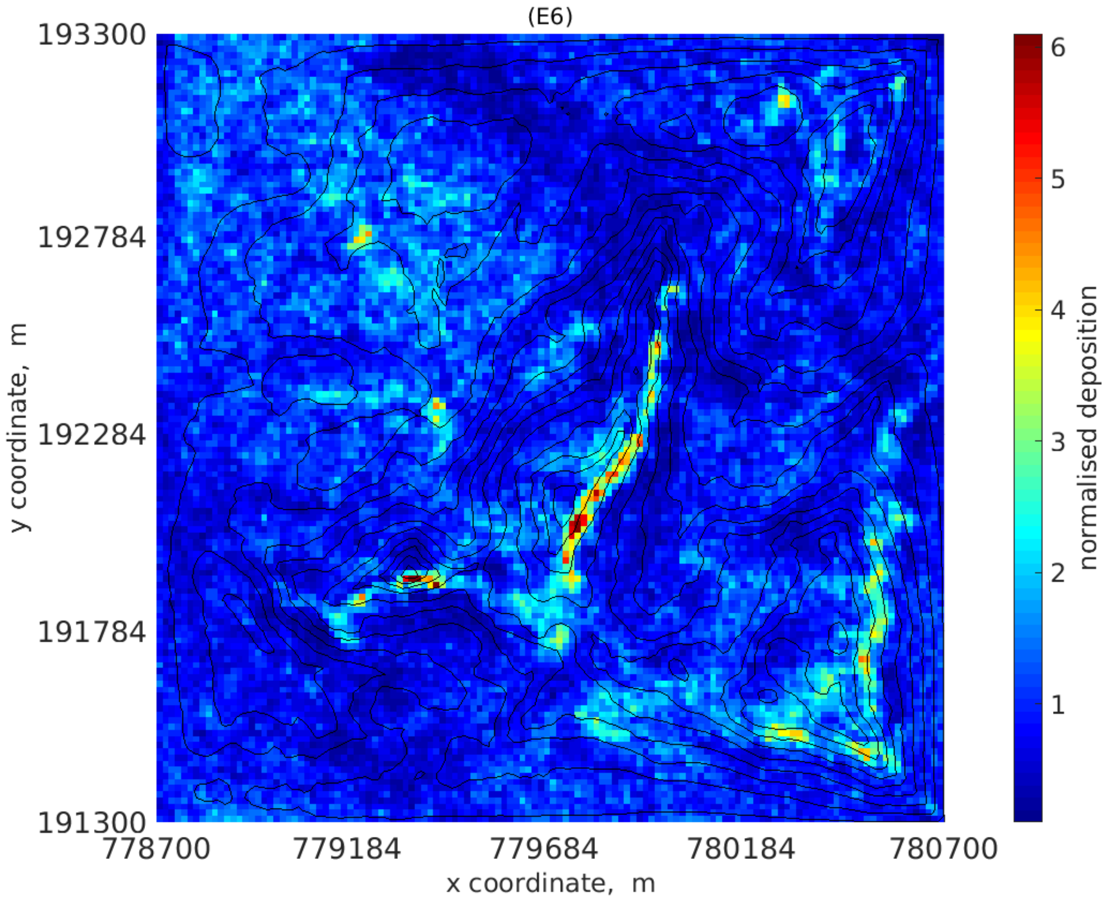

Figure 5.36: Normalised deposition and (height) contour lines. Snow particles without inertia, simulation E6.

Comparing deposition of inertia-less particles (Figure 5.36) to previous reference simulation (E1)(Figure 5.17) we notice that the normalised value of deposition doubled in the peak points while it remains around 1 in all the flatter region around the diagonal main ridge. Moreover local maxima appear here in the centre of our region and also, in the SW formation. With respect to E1, in E6 there are also enhanced accumulation zones on the high elevation area in the SE corner, as well little localized points in the land NW the Gaudergrat.

5.4 Dendritic Particles effect on preferential deposition

An important simplification of our model (Section4) is the precipitation particles shape. In simulations from E1 to E6 we assumed spherical grains with an equivalent diameter of 2 mm and a density of 500 kg/m^3, which is an effective density that partially accounts for the non-spherical shape. Here, we investigate how dendritic[2] snowflakes would interact with the flow and near-surface turbulence. We account for dendritic shape with a modified drag law that considers the effect of particle shape through empirical parameters (see, in Section 2.4 the correction to Equation 2.8 proposed by Loth [2008])

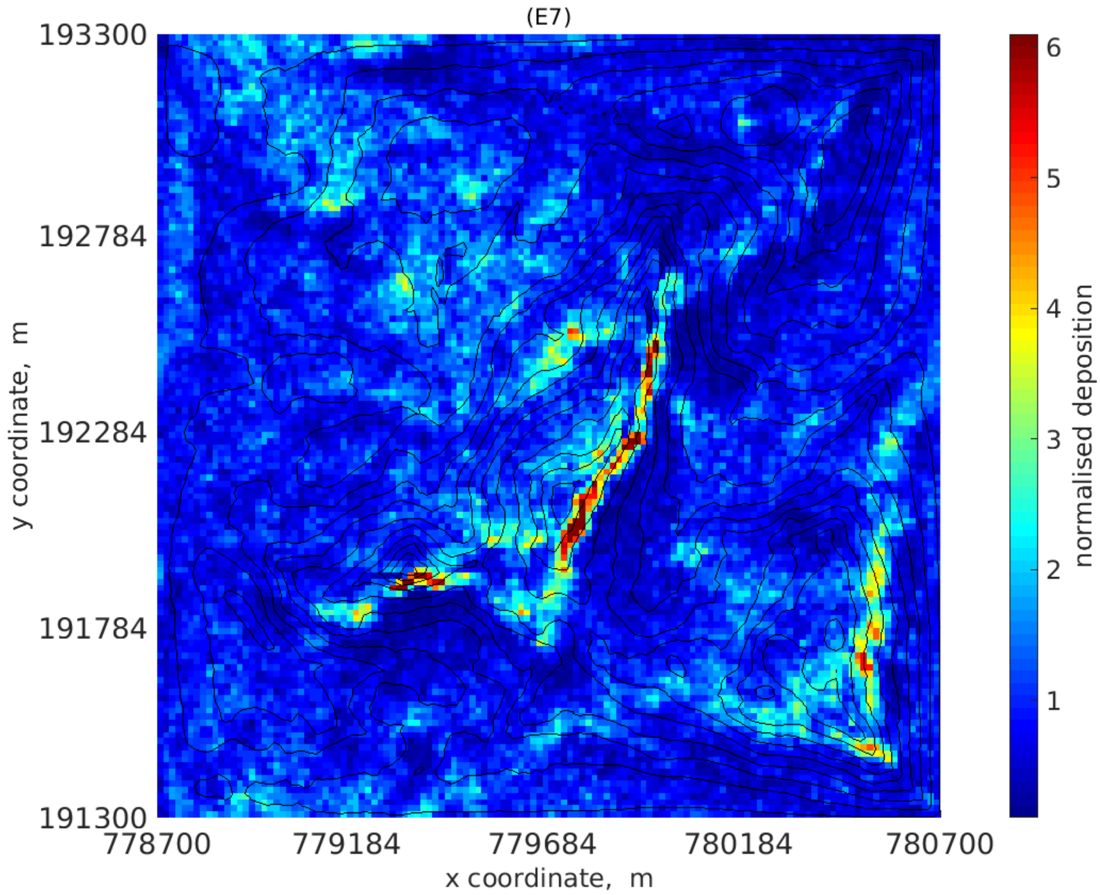

Figure 5.37: Normalised deposition and (height) contour lines. Dendritic snowflakes, simulation E7.

The resulting deposition (Figure 5.37) is more similar to E6 and E5 than to E1. We observe, in fact, enhanced deposition all along the diagonal mountainous formation, with local maxima just after the Gaudergrat summit and on the SE corner. Other localised zones of large accumulation precede the Gaudergrat ridge (following the wind inlet).

Finally we can look at Figure 5.38 to have a comprehensive view of how increasing velocity affects deposition profiles as well as inertia of particles or their dendritic shape do. Three

[2]under super-saturated conditions, and below-zero temperatures snowfall crystals form, assuming particularly symmetric (stellar or hexagonal) shapes

topographic sections are shown for snow depth distributions coming from simulations E1 to E7.

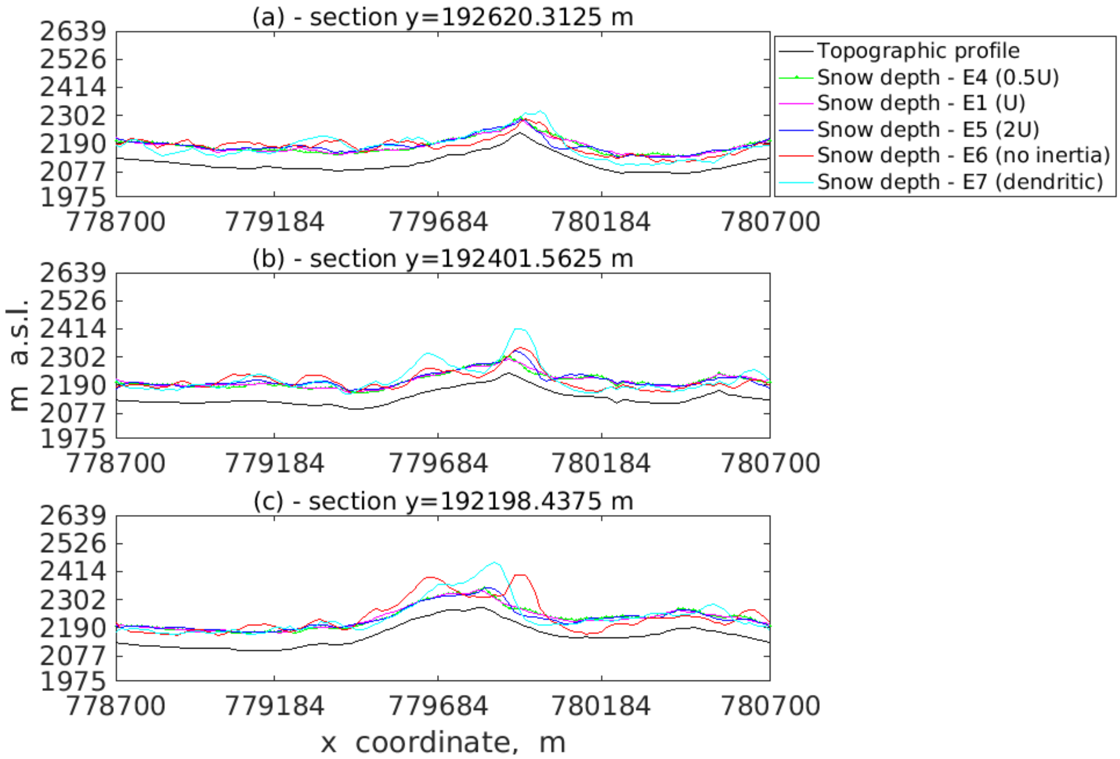

Figure 5.38: Normalised snow depth for increasing velocity (E1, E4, E5), for inertia-less particles (E6) and dendritic snow flakes (E7). (a) Section (S4), (b) Section (S3), (c) Section (S1).

5.5 Comparison of model results and available measurements

In this section we compare available snow depth measurements and simulation output with the qualitative purpose to understand to what extent preferential deposition can explain the total snow depth spatial variability. We are considering data manually collected from Lehning et al. [2008] before and after a big snow storm occurred in the period January-February 1999 which caused many avalanches phenomena. The location of these measurements points is shown in Figure 5.39. We compared the measured with the modelled deposition data obtained from case E1 (reference velocity), E5 (doubled velocity field intensity), E6 (no inertia particles), E7 (dendritic snowflakes). It is worth noting that the snow depth measurements include both precipitation and drifting snow, which is not accounted for in the numerical model. We normalised the two dataset compared (i.e. measurements and simulated) in order to have differences of them included in a range [-1 1] which allows to understand if the model overestimates (value 1) or underestimates (value -1) the real final snow distribution.
In Figure 5.40 we can have a first idea of how different flow conditions or model assumptions affect results. This figure simply tells where model overestimates or underestimated measured

data. In Figure 5.41 we can observe more into detail that the model tends to overestimate real snow depth preferably in the windward slope of the crest and more heavily for moderate velocity field intensity (E1 than E5). Extreme values of overestimation or underestimation decrease with the hypothesis of inertia less particles (in absence of snow drifting). Best fitting between predicted snow deposition (in absence of drifting and blowing snow) and field measurements are when dendritic snowflakes are simulated: colors hardly never reach extreme values thus they indicate slight underestimation by the model.

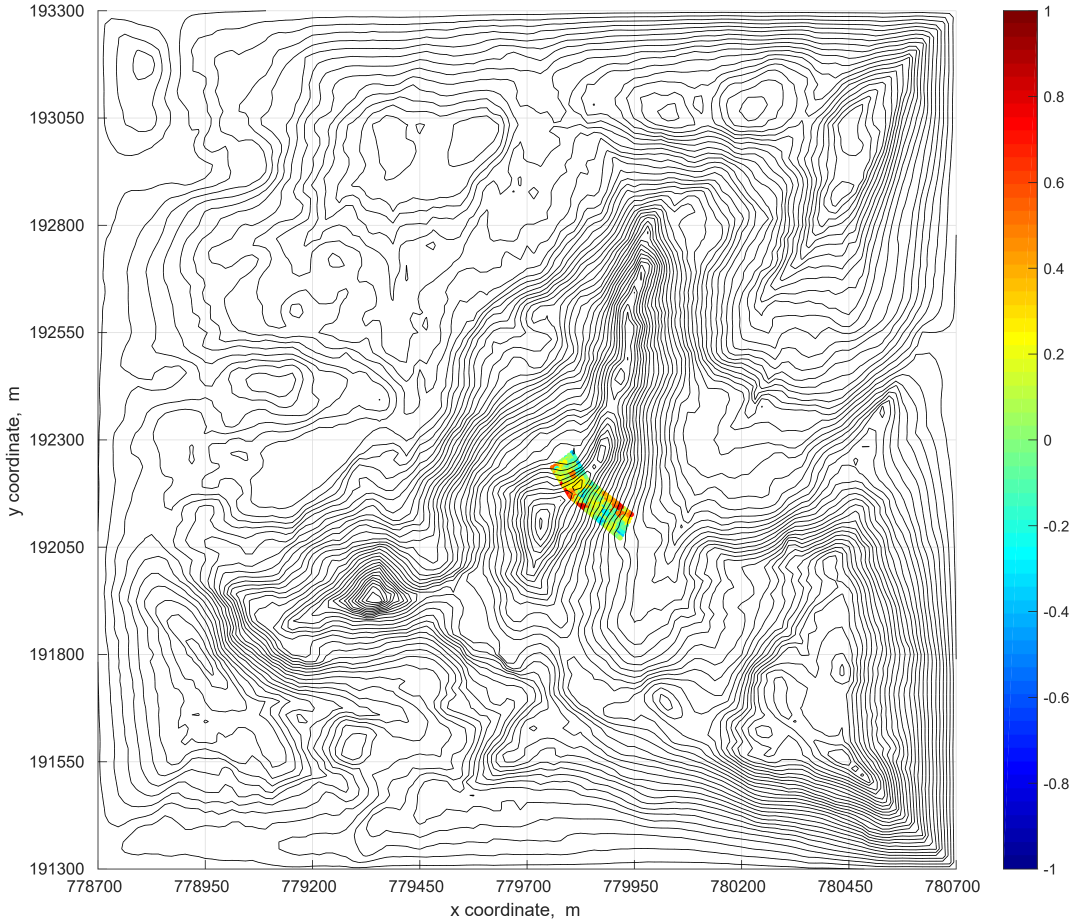

Figure 5.39: Measurement points location.

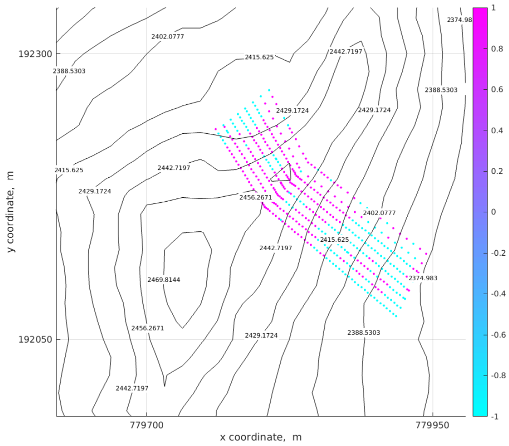

(a) Measured - E1.

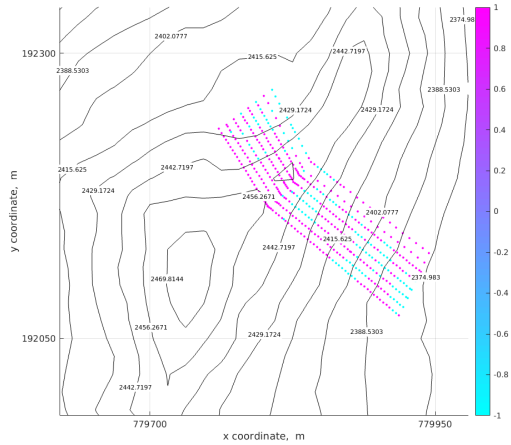

(b) Measured - E5.

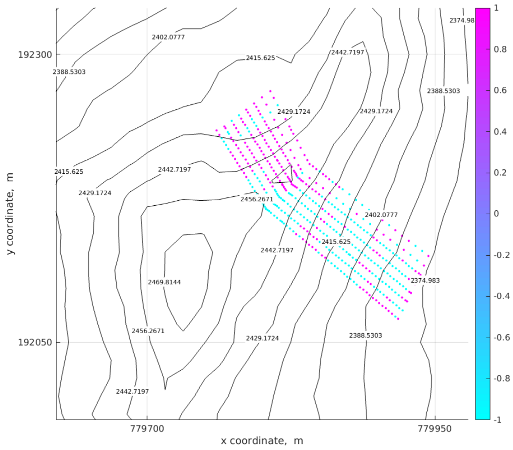

(c) Measured - E6.

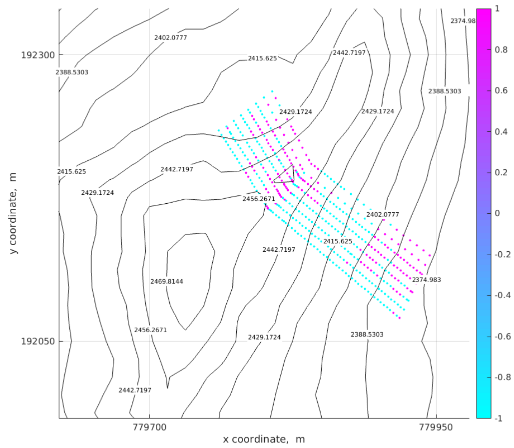

(d) Measured - E7.

Figure 5.40: Comparison of measured deposition values with (a) reference case; (b) doubled velocity field intensity; (c) inertia-less particles; (d) dendritic particles. Normalised datasets. Model overestimation if 1, model underestimation if -1.

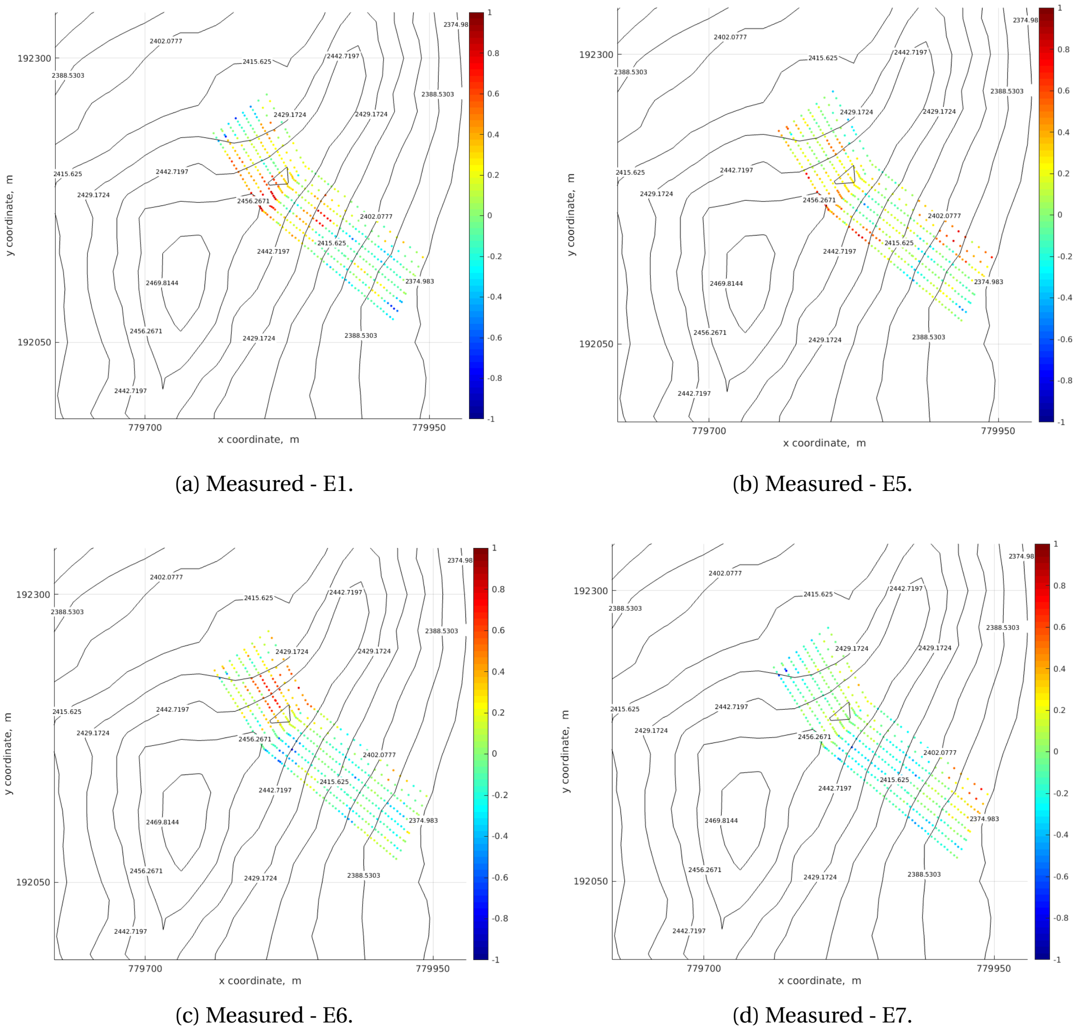

(a) Measured - E1.

(b) Measured - E5.

(c) Measured - E6.

(d) Measured - E7.

Figure 5.41: Comparison of measured deposition values with (a) reference case; (b) doubled velocity field intensity; (c) inertia-less particles; (d) dendritic particles. Normalised datasets.

These results suggest that the real snowcover after a snowfall in nature can be significantly affected also by sublimation or the strong wind effect which activates drifting and blowing snow eroding the just deposited snowcover.

6 Conclusions

The heterogeneous distribution of snow depth in alpine terrain is a matter of great interest for hydrology (estimation of SWE and run-off timing for drinking water and hydropower production), avalanche forecasting and little scale flow-particle interactions studies. The snow-cover is the result of many processes acting at different scales and time. In this work we investigated a near surface phenomenon called preferential snowfall deposition, that is the effect of near surface topography-induced turbulence on snowfall in absence of wind erosion, drifting and blowing of snow. Because the near-surface wind field is the main driver of heterogeneous snowfall deposition, especially on steep terrain, we used our LES-IBM-LSM model to perform simulations of snowfall deposition on a alpine topography (Gaudergrat ridge, Davos, Switzerland). We initially performed a sensitivity analysis of the model to the domain size and its periodic boundary conditions (E1, E2, E3 as in Table 4.1) and observed no significant effects on the snow depth spatial distribution around the Gaudergrat ridge, located in central part of the computational domain. We thus chose E1 (*Gaudergrat1*) as the reference case, which offers best trade off between accuracy and spatial resolution. Then we conducted a sensitivity analysis of the model to the flow intensity (E1, E4, E5 as in Table 4.2). We observed that, for a velocity field of 7 m/s, the snow cover distribution presents clear preferential deposition patterns that become more and more visible for higher velocity (14 m/s). For low wind gravity is the main driver of particles dynamics and the deposition tends to be more homogeneous. On the contrary, for high wind (and high Fr values) the control of flow advection of particle dynamics increases and the typical deposition pattern is an alternation of low and high deposition zone across the ridge. On the Gaudergrat, which is a fairly 45° oriented sharp ridge (SW-NE), we observe a nearly homogeneous deposition area in the windward side before the ridge, a remarkable (blue) line of low deposition in correspondence of the summit, followed by a clear (yellow-red) line of peak deposition and a more extended leeward area of low deposition (mainly for the E5) due to the sheltering effect of the mountain (Figure6.1). The more the snowfall is driven by advection, the more cornices-like formations and accumulation peaks on and beyond the crest occur. Results generated by the higest wind field intensity and Froude number (E5) have been compared with measured data ([Lehning et al., 2008]) in order to understand to what extent preferential deposition contributes to natural snow depth distribution. Normalising both datasets we find that the pure preferential deposition can not completely explain the spatial variability of snow on the alpine terrain. This, in fact, is the result of large and little scale phenomena (as orographic precipitation and flow-particle interactions: drifting, erosion, splash,..) which, for increasing velocity (and Fr number), lead to a decreased deposition on the windward side of the crest respect what predicted by our model. Other factors playing a role in the preferential snowfall deposition are the inertia of snow particles which interact with the close-surface wind flow, and their shape. Most of previous studies ([Lehning et al., 2008], [Mott and Lehning, 2010], [Mott et al., 2010]) assumed either inertialess particles or spherical grains. We then wanted to investigate to what extent these particle-related factors influence the deposition pattern under flow conditions described for E1. Noting that particle relaxation time becomes smaller for dendritic snowflakes and goes to zero for inertialess snow grains, we observe a much higher response of the particles to the flow variation (Figure 5.38). This results in doubled maxima deposition values (Figure 5.36 and Figure 5.37 vs Figure 5.17), higher snow depth variability across the ridge and shifting of maxima deposition location after the summit (Figure 5.38) respect E1-E5. In particular, the highest deposition is on the massive central part of the Gaudergrat (779700 m E); windward side enhanced deposition is visible below the latitude of 192284 m N especially for dendritic snowflakes. For inertia-less particles deposition, it is less easy to recognise the sheltering effect beyond the ridge (following the flow direction) than in E5. We can still notice a certain similarity in deposition pattern resulting from E1 and E6 thus local maxima differences are not negligible. For the flow intensity investigated, we found the same range of deposition value and similar pattern in E5 and E7 thus dendritic snowflakes lead to an higher wind ward and summit deposition (Figure6.1) [Comola et al., in preparation].

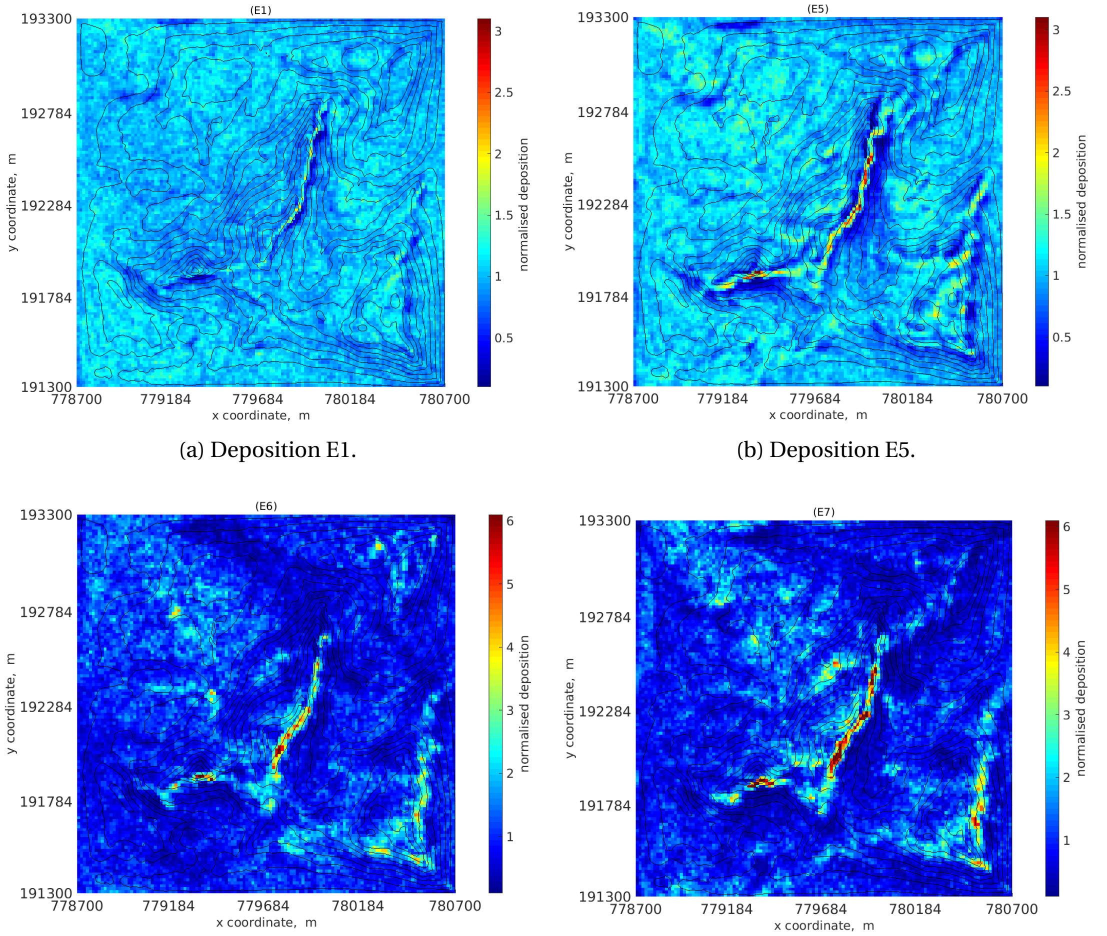

(a) Deposition E1.

(b) Deposition E5.

(c) Deposition E6.

(d) Deposition E7.

Figure 6.1: Snow deposition for (a) reference case; (b) doubled velocity; (c) inertia-less particles; (d) dendritic particles.

With respect to the initial results of Lehning et al. [2008], some progress has been done in the coupling between the atmospheric and drift models, in the improvement of the computational grid resolution (from 25 m to 15.6 m, horizontal) and in the implementation of all near-surface processes. Nevertheless the numerical grid resolution of this LES-IBM-LSM application is still only sufficient for preferential deposition investigation and not for solving drifting snow trajectories, which are mostly ballistic trajectories very close to the ground. Regarding the sensitivity of preferential deposition process to the wind intensity, this work confirmed and extended what was observed from previous findings, such as the scale analysis of Comola et al. [in preparation] and the results obtained by Mott et al. [2014] and Lehning et al. [2008]. About the influence of particle-related factors as inertia and shape on preferential deposition, results seem to suggest that the assumption of inertialess particles, often made in previous studies, could provide effective prediction of grain deposition. On the other hand the assumption of spherical particles could provide potentially erroneous results: as seen in Figure 5.41 the simulation of dendritic snowflakes deposition better reproduces measured data among the four.

Future work includes unravelling the relative contribution of preferential deposition and drifting snow on the total snow depth spatial variability in order to decrease the dis-match between field measurements (drift affected) and model results. Our results in fact also point toward the need for more accurate and spatially distributed measurements of snow deposition over complex terrain. Finally, a phenomenon that we did not discuss or take in to account modelling preferential deposition with this LES-IBM-LSM numerical model is snow sublimation which can explain overestimation of snow depth at such a local scale [Groot Zwaaftink and Lehning, 2010].

Bibliography

J. D. Albertson and M. B. Parlange. Surface length scales and shear stress: Implications for land-atmosphere interaction over complex terrain. *Water Resources Research*, 35(7):2121–2132, 1999.

E. Bou-Zeid, C. Meneveau, and M. Parlange. A scale-dependent lagrangian dynamic model for large eddy simulation of complex turbulent flows. *Physics of fluids*, 17(2):025105, 2005.

R. Clift, J. R. Grace, and M. E. Weber. *Bubbles, drops, and particles*. Courier Corporation, 2005.

B. A. Colle, R. B. Smith, and D. A. Wesley. Theory, observations, and predictions of orographic precipitation. In *Mountain Weather Research and Forecasting*, pages 291–344. Springer, 2013.

F. Comola. Stochastic modeling of snow transport and hydrologic response in alpine terrain. 2017.

F. Comola, M. G. Giometto, S. T. Salesky, M. B. Parlange, and M. Lehning. Scale analysis of snowfall deposition over complex terrain using large eddy simulations and lagrangian stochastic modeling. *Journal of Fluid Mechanics*, in preparation.

T. J. Garrett and S. E. Yuter. Observed influence of riming, temperature, and turbulence on the fallspeed of solid precipitation. *Geophysical Research Letters*, 41(18):6515–6522, 2014.

M. Giometto, A. Christen, C. Meneveau, J. Fang, M. Krafczyk, and M. Parlange. Spatial characteristics of roughness sublayer mean flow and turbulence over a realistic urban surface. *Boundary-Layer Meteorology*, 160(3):425–452, 2016.

D. Goossens. Wind tunnel experiments of aeolian dust deposition along ranges of hills. *Earth Surface Processes and Landforms*, 21(3):205–216, 1996.

C. Groot Zwaaftink and M. Lehning. Modelling sublimation of drifting snow in an alpine catchment and investigating temperature and moisture feedbacks. In *10th EMS Annual Meeting, 10th European Conference on Applications of Meteorology (ECAM) Abstracts, held Sept. 13-17, 2010 in Zürich, Switzerland. http://meetings. copernicus. org/ems2010/, id. EMS2010-295*, 2010.

A. N. Kolmogorov. The local structure of turbulence in incompressible viscous fluid for very large reynolds numbers. In *Dokl. Akad. Nauk SSSR*, volume 30, pages 299–303, 1941.

V. Kumar, J. Kleissl, C. Meneveau, and M. B. Parlange. Large-eddy simulation of a diurnal cycle of the atmospheric boundary layer: Atmospheric stability and scaling issues. *Water resources research*, 42(6), 2006.

M. Lehning, H. Löwe, M. Ryser, and N. Raderschall. Inhomogeneous precipitation distribution and snow transport in steep terrain. *Water Resources Research*, 44(7), 2008.

E. Loth. Drag of non-spherical solid particles of regular and irregular shape. *Powder Technology*, 182(3):342–353, 2008.

K. N. M. Nemoto. Numerical simulation of snow saltation and suspension in a turbulent boundary layer. *Journal of geophysical research*, 109(di18206):1–14, 2004. doi: 10.1029/2004JD004657.

C. Magono and T. Nakamura. Aerodynamic studies of falling snowflakes. *Journal of the Meteorological Society of Japan. Ser. II*, 43(3):139–147, 1965.

C. Meneveau, T. S. Lund, and W. H. Cabot. A lagrangian dynamic subgrid-scale model of turbulence. *Journal of Fluid Mechanics*, 319:353–385, 1996.

R. Mott and M. Lehning. Meteorological modeling of very high-resolution wind fields and snow deposition for mountains. *Journal of Hydrometeorology*, 11(4):934–949, 2010.

R. Mott, M. Schirmer, M. Bavay, T. Grünewald, and M. Lehning. Understanding snow-transport processes shaping the mountain snow-cover. *The Cryosphere*, 4(4):545, 2010.

R. Mott, D. Scipion, M. Schneebeli, N. Dawes, A. Berne, and M. Lehning. Orographic effects on snow deposition patterns in mountainous terrain. *Journal of Geophysical Research: Atmospheres*, 119(3):1419–1439, 2014.

S. A. Orszag and Y.-H. Pao. Numerical computation of turbulent shear flows. *Advances in Geophysics*, 18:225–236, 1975.

R. E. Passarelli Jr and R. C. Srivastava. A new aspect of snowflake aggregation theory. *Journal of the Atmospheric Sciences*, 36(3):484–493, 1979.

S. B. Pope. Turbulent flows, 2001.

F. Porté-Agel, C. Meneveau, and M. B. Parlange. A scale-dependent dynamic model for large-eddy simulation: application to a neutral atmospheric boundary layer. *Journal of Fluid Mechanics*, 415:261–284, 2000.

M. Reeks. The transport of discrete particles in inhomogeneous turbulence. *Journal of aerosol science*, 14(6):729–739, 1983.

S. Salesky, M. Giometto, M. Chamecki, M. Lehning, and M. Parlange. The transport and deposition of heavy particles in complex terrain: an eulerian model for large eddy simulation. *submitted to Water Resources Research*, 2016.

J. Schweizer, J. Bruce Jamieson, and M. Schneebeli. Snow avalanche formation. *Reviews of Geophysics*, 41(4), 2003.

D. Scipión, R. Mott, M. Lehning, M. Schneebeli, and A. Berne. Seasonal small-scale spatial variability in alpine snowfall and snow accumulation. *Water resources research*, 49(3):1446–1457, 2013.

V. Sharma, M. Parlange, and M. Calaf. Perturbations to the spatial and temporal characteristics of the diurnally-varying atmospheric boundary layer due to an extensive wind farm. *Boundary-Layer Meteorology*, 162(2):255–282, 2017.

R. B. Stull. *An Introduction to Boundary Layer Meteorology*. International series of monographs on physics. Clarendon Press, 2009. ISBN 9789027727695.

D. Thomson. Criteria for the selection of stochastic models of particle trajectories in turbulent flows. *Journal of Fluid Mechanics*, 180:529–556, 1987.

Y.-H. Tseng, C. Meneveau, and M. B. Parlange. Modeling flow around bluff bodies and predicting urban dispersion using large eddy simulation. *Environmental science & technology*, 40 (8):2653–2662, 2006.

L. Verlet. Computer "experiments" on classical fluids. i. thermodynamical properties of lennard-jones molecules. *Physical review*, 159(1):98, 1967.

V. Vionnet, E. Martin, V. Masson, C. Lac, F. Naaim Bouvet, and G. Guyomarc'h. High-resolution large eddy simulation of snow accumulation in alpine terrain. *Journal of Geophysical Research: Atmospheres*, 122(20), 2017.

Z. Wang and N. Huang. Numerical simulation of the falling snow deposition over complex terrain. *Journal of Geophysical Research: Atmospheres*, 122(2):980–1000, 2017.

J. C. Weil, P. P. Sullivan, and C.-H. Moeng. The use of large-eddy simulations in lagrangian particle dispersion models. *Journal of the atmospheric sciences*, 61(23):2877–2887, 2004.

J. D. Wilson. Trajectory models for heavy particles in atmospheric turbulence: comparison with observations. *Journal of Applied Meteorology*, 39(11):1894–1912, 2000.

A. Winstral, K. Elder, and R. E. Davis. Spatial snow modeling of wind-redistributed snow using terrain-based parameters. *Journal of Hydrometeorology*, 3(5):524–538, 2002.